Microstructural and microhardness variations of laser powder bed fusion (L-PBF) additively manufactured Inconel 718 due to machine variability and wall thickness for aerospace applications

A. Doris[1,3], L. Trujillo[1,3], D. Godinez, E. Arrieta[1,2], R.B. Wicker[1,2], P. Gradl[4], C.C. Katsarelis[4], and F. Medina[1,2]

[1] W.M. Keck Center for 3D Innovation, The University of Texas at El Paso, El Paso, TX 79968, USA
[2] Department of Aerospace and Mechanical Engineering, The University of Texas at El Paso, TX 79968, USA
[3] Department of Metallurgical, Materials, and Biomedical Engineering, The University of Texas at El Paso, TX 79968, USA
[4] NASA Marshall Space Flight Center, Huntsville, Al, 35812, USA
* Corresponding author (adoris@miners.utep.edu)

ABSTRACT

This paper reports on a study investigating the microstructure and microhardness of thin walls fabricated by Laser Powder Bed Fusion (L-PBF) from sixteen geometric feature build plates. The study evaluated any variance in those properties with the variation in thickness by characterizing the XY and YZ planes of seven thin walls of different thicknesses and the base parts. Electron Backscatter Diffraction (EBSD) analysis with inverse pole figure (IPF) mapping was done for four samples from four different machine manufacturers. From the EBSD grain boundary map, the microstructure is composed of equiaxed grains with a lower threshold angle with smaller grains in the border area. Compositional analysis for both the powders and the resulting fully heat-treated L-PBF manufactured material was analyzed for alloy element stability and contaminants using 10 mg samples. The paper concludes by showing the relationship between composition and microstructural properties.

Keywords: Inconel 718, Laser powder bed fusion (L-PBF), Geometric feature build plate, Multiple machine configurations, Heat treatment, Microindentation hardness, Optical microscopy and EBSD image mapping, Microstructure.

_____

1. Introduction

While metal additive manufacturing (AM), especially laser powder bed fusion (L-PBF) fabrication of products and components having complex internal and external geometries, has demonstrated a wide range of advantages over more traditional manufacturing [1-7], there remain many unknowns to address. A majority of L-PBF studies have examined residual, as-built

microstructure-property relationships [8-11] as well as those associated with post-process heat treatment [12-17]. However, many practical applications of AM processing for industrial, automotive, and aerospace fields lack a fundamental understanding of geometric feature reproducibility between various AM machine configurations, machine-to-machine variability, and interrelationships between microstructure-property-product design geometry. In this context, end-use AM product performance can be defined by an understanding of microstructure-property geometry control; including geometric tolerances, as these relate to build-process limitations and process parameters.

It is well established that the thickness of metallic components, along with grain size, has an effect on mechanical properties [18-22]: thicker samples, even with large grain sizes, tend to exhibit higher yield strengths. With the development and applications of additive manufacturing technologies, the ability to fabricate complex component geometries has drawn attention to the effect of the related geometrical thicknesses on the mechanical performance of such parts. In addition, the building strategies and processing parameters required in optimizing component microstructures in relation to the build geometries become important in the context of different AM processes and the specific machine performance features; especially machine-to-machine variability as noted above. While there have been a number of studies involving the effects of build geometry (and especially component geometry thickness) on the microstructure and mechanical properties of a range of metals and alloys fabricated by laser powder bed fusion [18-22, 23-28], there are no comprehensive studies of such effects over a wide range of part thicknesses; and for a wide range of commercially available AM (LPBF) machines.

In a recent study by Gradl, et al. [29], a series of Inconel 718 LPBF manufactured geometric feature build plates to baseline were evaluated for variations between different LPBF machine configurations. The study completed 16 different builds using an identical CAD file across 15 different machines installed at 12 different locations; utilizing Inconel 718 alloy. The geometric feature build plate included round holes, concentric, hollow, and protruding cylinders, square channels, freeform surface and slots, and a range of wall thicknesses ranging from nominally 0.1 mm to 2 mm. Features from the build plates were measured using optical and mechanical methods, and the systematic error for build accuracy across all features was 25.8 +/- 5.5 microns; with a 99.9 % confidence interval. However, as comprehensive as this study demonstrated, there were no corresponding microstructure and mechanical property measurements and no microstructure-property-geometry control assessments.

The present study utilizes the same 16 geometric feature build plates built across 15 different LPBF machines; using Inconel 718 alloy as in the study by Gradl, et al. [29]. However, the present study focused on nominal feature thicknesses ranging from 0.1 to 2.0 microns in build plates variously heat treated by stress relief (SR) anneal at 1066 ℃, SR + HIP at 1163 ℃, and fully heat treated (FHT) plates characterized by SR + HIP + solution anneal (SOL) at 1066 ℃ + double aging (AGE) at 760 ℃ and 649 ℃; for appropriate times and cooling conditions. The microstructures, especially grain size features along with corresponding microindentation hardnesses were measured and compared for these variously heat-treated build artifact/part thicknesses in both the build direction and perpendicular to the build direction (utilizing planes parallel and perpendicular to the build direction: YZ and XY, respectively). Microstructure observations were made using optical metallography and EBSD mapping, while microindentation hardness was measured using Vickers (HV) indentation.

2. Materials and methods

2.1 Feature build plate description

Sixteen L-PBF AM Inconel 718 build plate artifacts (Table 1) were received in variously heat-treated conditions, including Stress Relief (SR), SR + Hot Isostatic Pressing HIP), and fully heat treated condition (FHT): SR + HIP + Solution +Aged (SOL, AGE) conditions. The build plates and geometric features underwent stress relieving at 1066 ˚C for 90 min and slow cooling in the furnace according to ASTM F3055-14a. The HIP was completed per standard ASTM 3301-18a, and the solution and 2-step aging per AMS 5664. The nominal dimensions of the feature build plate were 140 mm in X-orientation, 140 mm in Y-orientation, and 32 mm in Z-height. The feature build plate volume was 143 cm³, associated with a surface area of 722 cm² and a mass of 1.34 kg. The geometric features include varying angle walls; X- and Y- distances; horizontal holes; and vertical features, including round holes, concentric hollow cylinders, protruding cylinders, thin wall thickness, square channels, freeform surface, and slots. The base layer of Inconel 718 containing all the features was 3.81 mm in thickness [29].

The thin vertical walls being studied in this paper ranged from 0.10 to 2.0 mm in nominal width. Not all the walls were built successfully, especially the thinnest wall (No.1) wall at 0.1 mm, which or most of the build plates failed completely, partially built, or were thicker than designed. Only four machine configurations appeared to successfully build the 0.10 mm wall, including plates referenced as 7, 10, 11, and 12 (Table 2). The smallest two wall widths, nominally 0.10 mm and 0.20 mm in thickness, were subjected to complete failure or curling in most cases. An isometric view of the sample build design with all the geometric features is shown in Fig 1. Information from service vendors regarding machine configurations and build parameters have been listed in Table 1, which was provided in the previous study by Gradl et al. [29]. The varying wall thicknesses specifically studied in this paper have been included in Table 2. The thicknesses were measured with a digital slide caliper by taking an average of five measurements for each wall. The measurements exclude the curled or failed parts' value to better illustrate the deviation for the universally successful builds. The deviation ranged between +178/-152 µm and the mean from 0 µm to 25 µm for universally successful builds [29].
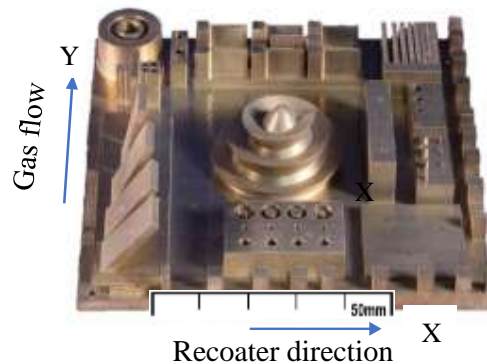

Fig 1: L-PBF additively manufactured Inconel 718 feature build plate artifact sample.

Table 1: Machine overview from shared information of vendor build parameters.

ID	Machine Model Type	Layer Height (µm)	Recoater Type	Power (W)	Scan Speed (mm/s)	Energy Density (J/mm³)	Core Scan Strategy
1	EOS M400	40	Rubber	285	960	74.2	Stripes
2	EOS M280	40	Steel	-	-	-	Stripes
3	EOS M280	40	-	-	-	-	-
4	EOS M290	40	Carbide Knife	285	960	74.2	Stripes
5	EOS M280	40	Brush	285	960	74.2	Stripes
6	EOS M280	40	Soft Recoater	285	960	74.2	Stripes
7	**Concept M2**	**30**	**Rubber**	**180**	**600**	**95.2**	**Checkered**
8	EOS M280	40	High-Speed Steel	285	960	74.2	Stripes
9	EOS M290	40	EOS Steel	285	900	-	Stripes
10	**SLM280**	**30**	**Silicone**	**200**	**900**	**61.7**	**Stripes**
11	SLM280 Dual	30	Silicone	200	900	61.7	Stripes
12	**Velo Sapphire**	**50**	**Non-Contact**	**-**	**-**	**-**	**Checkered**
13	EOS M290	40	Carbon	285	960	74.2	Stripes
14	EOS M290	40	Steel	285	960	74.2	Stripes
15	EOS M280	40	Carbon Fiber Brush	285	960	74.2	Stripes
16	**EOS M290**	**40**	**Carbon Fiber Brush**	**285**	**960**	**74.2**	**Stripes**

Table 2: Varying Thicknesses of Vertical Thin Walls.

		Per Specifications: Vertical Thin Walls, Varying Thicknesses (mm)						
Wall ID		1	2	3	4	5	6	7
Nominal Thickness		0.10	0.20	0.41	0.61	0.81	1.02	2.03
Machine	**Build plate Identifier**	Vertical Thin Walls, Varying Thicknesses (mm)						
EOS M400	1	0.22	0.32	0.46	0.64	0.83	1.02	2.04
EOS M280	2	-	0.25	0.42	0.61	0.80	1.00	2.04
EOS M280	3	-	0.19	0.36	0.55	0.74	0.97	1.98
EOS M290	4	0.14	0.22	0.34	0.55	0.75	0.94	1.96
EOS M280	5	-	0.28	0.43	0.61	0.83	1.02	2.03
EOS M280	6	-	0.14	0.37	0.53	0.74	0.94	1.93
Concept M2	**7**	**0.22**	**0.33**	**0.39**	**0.44**	**0.79**	**1.05**	**2.13**
EOS M280	8	0.22	0.19	0.37	0.56	0.76	0.97	1.98

EOS M290	9	-	0.29	0.42	0.61	0.84	1.02	2.03
SLM280	**10**	**0.20**	**0.24**	**0.39**	**0.61**	**0.83**	**1.02**	**2.03**
SLM280-Dual	11	0.22	0.36	0.36	0.55	0.80	0.95	2.04
VELO Sapphire	**12**	**0.19**	**0.17**	**0.30**	**0.58**	**0.77**	**0.98**	**2.03**
EOS M290	13	0.11	0.28	0.39	0.61	0.81	1.00	2.01
EOS M290	14	0.14	0.20	0.38	0.58	0.80	0.99	2.02
EOS M280	15	-	0.25	0.38	0.57	0.79	0.98	1.99
EOS M290	**16**	**0.14**	**0.25**	**0.43**	**0.62**	**0.83**	**1.02**	**2.03**
Average Deviation		0.08	0.05	0.03	0.04	0.03	0.02	0.03
Average		0.11	0.25	0.38	0.58	0.79	0.99	2.02
Standard Deviation		0.09	0.06	0.05	0.05	0.03	0.03	0.05

2.2 Heat treatment

The heat treatment schedules shown in Table 3 represent relatively standard post-processing treatments for both conventional and additively manufactured Inconel 718 over several decades [30]. This schedule included a stress-relief (SR) anneal following ASTM3055-14a standard which at a temperature of 1066 $^{\circ}$C initiated recrystallization of the as-built microstructures. HIP of the as-built components at 1163 $^{\circ}$C (ASTM 3301) provided both continued recrystallization and grain growth. These treatments solubilized existing precipitates and second-phase particles and provided a homogenized grain structure. Components were also fully heat-treated (FHT) by SR + HIP + solutionizing + double aging (AMS 5664), as shown in Table 3. The two-step aging process (AGE) re-precipitated primarily gamma double-prime, Ni_3Nb precipitates in the recrystallized, growing grains.

Table 3: Full heat-treatment (FHT): (SR+HIP+SOL+AGE) for all the samples

Stress Relief	1066 °C for 1.5 hrs in vacuum (ASTM 3055-14a)
HIP	1163 °C for 3-4 hours at 15ksi (ASTM 3301)
Solution	1065 ± 3 °C for 1h, cooling at a rate of air cooling or faster (AMS 5664)
Aging	760 ± 9°C for 10 h ± 0.5 h, furnace cool to 649 ± 9°C, hold at 649 ± 9°C until a total aging heat treatment time of 20 hours (AMS 5664)

2.3 Metallographic preparation

Sectioning samples revealed the build direction microstructure with an ATM Brilliant 220 precision cutter. Thin wall samples were sectioned in XY and YZ axes, where XY represents the plane normal to the build direction, and YZ refers to the plane in the build direction. Metallographic

samples of the sectioned specimens were created using a combination of powdered epoxy and phenolic acid and a hot mounting press from ATM OPAL (Haan, Germany). Grinding and polishing were done after the samples were mounted to produce a mirror-like surface.

The grinding and polishing procedures were conducted with an ATM SAPHIR 530 semiautomatic system. The grinding procedure started with a 320-grit coarse Si-C (Silicon carbide) grinding paper, followed by grits 600 and 800 each was spun at 200 RPM with a force of 25N for 2 minutes using water as a lubricant. The polishing procedure was carried out at a speed of 150 RPM and a force of 25 N for 3 minutes, with each stage of the polishing process having a different nylon disk for the 6 m, 3 m, and 1 m diamond slurries. The samples were ultrasonicated before polishing and in between each polishing stage to eliminate cross-contamination.

Kalling's No. 2 Reagent (2g $CuCl_2$, 40 ml HCl, 40-80 ml Ethanol) was used to etch the polished samples. Swabbing of the specimen with a cotton ball wet by the etching solution for a range of 45 to 90 seconds was the etching procedure in this investigation. The optical micrographs in this work were taken with an Olympus GX53 inverted optical microscope (Olympus Inc., Tokyo, Japan).
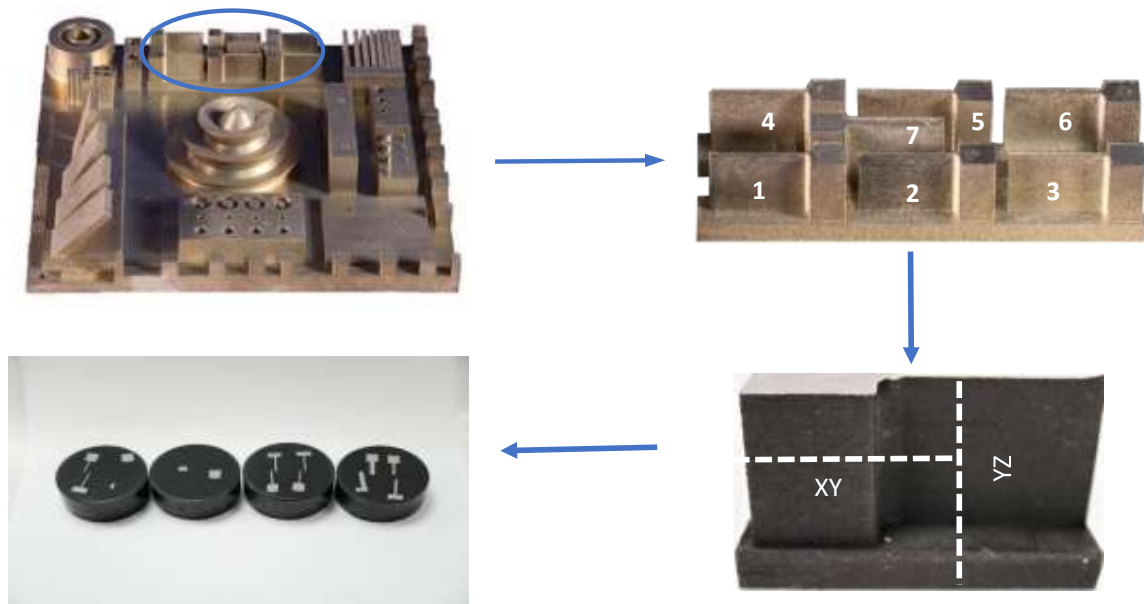
Fig 2: Sectioning and mounting of the thin wall parts.

2.4 Hardness testing

Micro-indentation hardness testing was completed using a Qness30 CHD Master[+] Microhardness tester according to ASTM E384. Indentations were made with a Vickers indenter and a load of 100 gf and measured with a 50X objective lens. At least five measurements were taken for each thin wall sample.

2.5 Grain width measurement

The grain width (or average grain size) measurements were calculated by the line intercept method, a process described in ASTM E112 [31]. ImageJ software was used to draw at least five straight lines (three lines parallel and two diagonally) across the micrograph of 200x magnification

at different angles for both XY and YZ planes and to count intercepted grain boundary numbers, including annealing twin boundaries. The average of five straight lines and five intersections was determined for each micrograph. The average grain width for each XY and YZ plane of sixteen samples was measured using the following formula:

$$Average\ Grain\ size\ (microns) = \frac{Average\ length\ of\ the\ straight\ lines\ (microns)}{Average\ number\ of\ intersections} \qquad (1)$$

2.6 EBSD analysis

Electron Backscatter Diffraction (EBSD) analysis utilizes specialized instrumentation, including a scanning electron microscope (SEM) and an EBSD detector, to acquire data through electron beam scanning and diffraction pattern collection [32]. The obtained data is then interpreted and analyzed to extract valuable information about microstructural properties, showing differences in terms of grain size, grain distribution (orientation), and twinning behavior [33)].

2.7 XRD analysis

X-Ray Diffraction (XRD) analysis involves exposing a sample to X-rays and analyzing the resulting diffraction pattern. By measuring the angles and intensities of the diffracted X-rays, valuable information about the crystal structure, phase composition, and lattice parameters of the material can be obtained. Fully heat-treated thin walls from machine manufacturer 290 were analyzed using Bruker D8 Discover XRD instruments. The obtained peak spectrum was modified using OriginPro software.

3. Results and discussion

3.1 Optical microscope analysis of LPBF built and heat-treated Inconel 718 thin sections

Figures 3 and 4 show examples of optical microscope imaging and analysis of thin section artifacts from one of the 16 LPBF fabricated Inconel 718 geometric feature build plates (see Fig. 2 and Table 1), which have been variously heat-treated and observed in both the XY plane (perpendicular to the build direction) and the YZ plane (parallel to the build direction), respectively. The stress relief (SR) annealed thin sections (TW-1 (0.1 mm) and TW-2 (0.2 mm)) exhibit some degree of columnar grain structure in the YZ plane parallel to the build direction, indicating incomplete recrystallization (Fig. 4), while the structure in the XY plane perpendicular to the build direction (Fig. 3) exhibits a fine-grain, equiaxed structure. As noted previously, the thinnest sections (nominally 0.1 mm) were not reliably built in all machine configurations (Table 3) as shown in Fig. 3 for the SR + HIP and fully heat-treated FHT samples in the XY plane views; and grain size measurements were often not representative for the 0.1 mm and 0.2 mm sections. The thinnest sections, 0.1 mm and 0.2 mm also exhibited more rapid cooling in the build process and refining the microstructure. Grain sizes for the 0.1 mm sections in the XY plane varied from ~ 21 microns to ~ 42 microns in contrast to ~ 25 microns to ~ 46 microns in the YZ plane. The HIP (SR + HIP) and FHT thin section feature plate samples shown in Figs. 3 and 4 illustrate more complete recrystallization, especially for section thicknesses > 0.4 mm as a consequence of the larger volume of heat retention and the higher temperature HIP (at 1163 °C), which induced grain growth of generally equiaxed grains containing annealing twins in Both the XY and YZ planes. Nominal grain sizes (including twins) were measured for the FHT thicker sections in Figs. 3 and 4 (between

0.41 mm and 2.03 mm nominal thickness) varied from ~ 34 microns to ~ 95 microns in the XY plane, and ~ 51 microns to ~ 77 microns in the YZ plane, respectively. A summary of measured grain sizes for all FHT build plate feature thicknesses is shown in Tables 4 and 5; corresponding to XY and YZ plane imaging, respectively. In addition, Figs 5 and 6, correspondingly attached to these tables provide a convenient graphical comparison of the grain sizes. Figures 5 and 6 illustrate the general trending of increasing grain size with increasing feature section thickness in both the XY and YZ plane orientations for all machine builds (Tables 1 and 2). It is also notable that the annealing twin density tends to decrease as the grain size increases (Figs. 3 and 4), consistent with observations of annealing twin density evolution during grain growth in Inconel 718 [34].
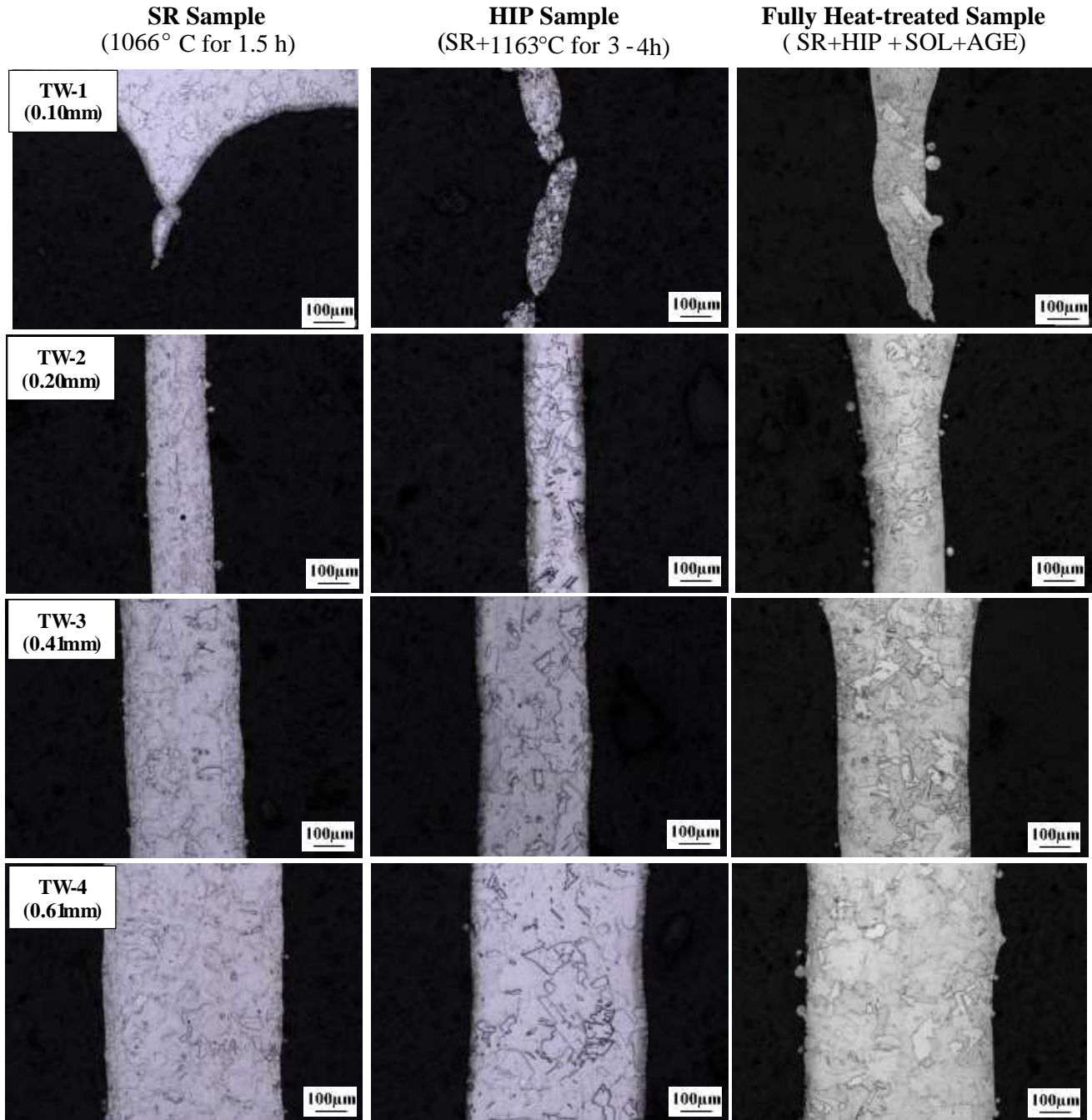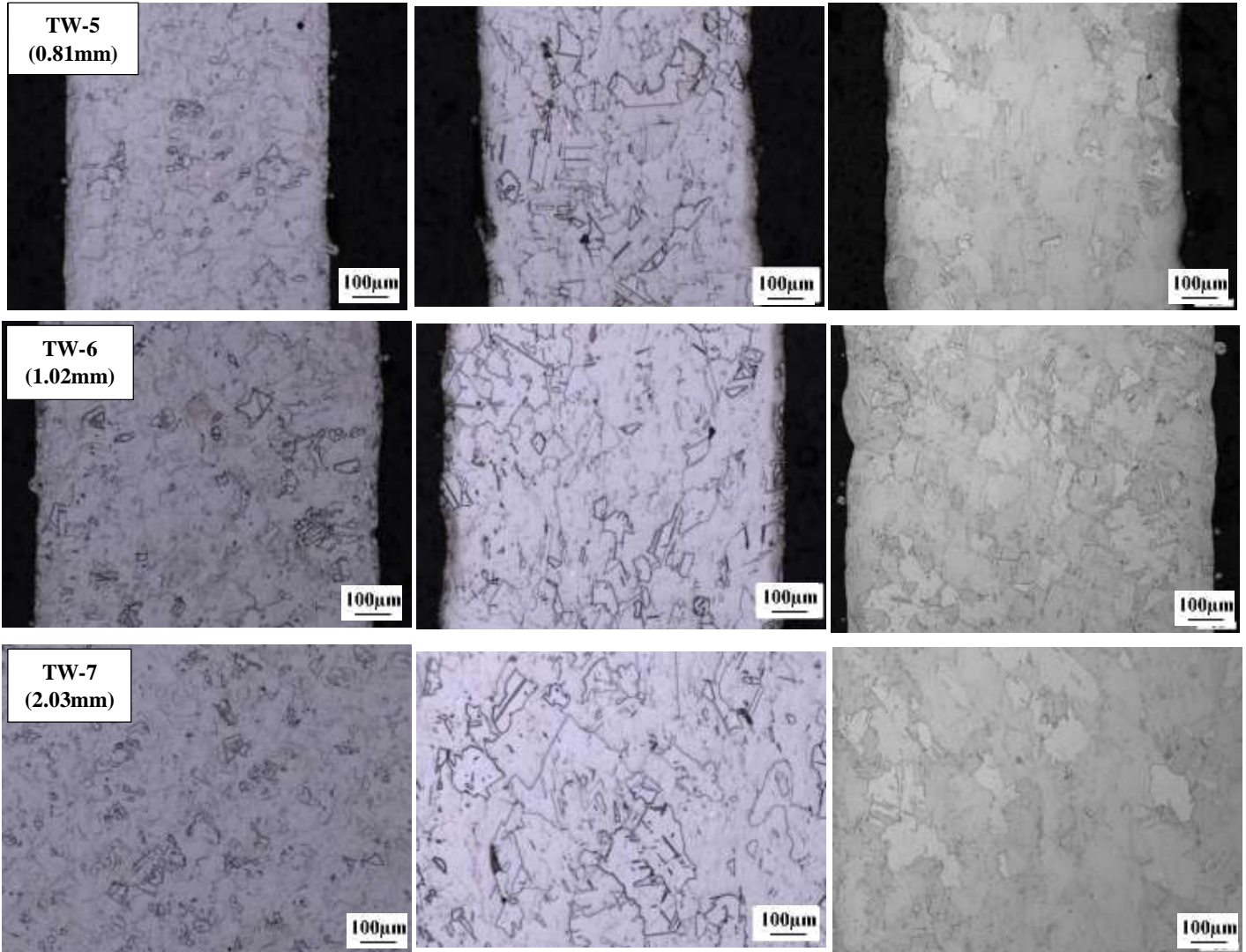

Fig 3: Microstructural comparison of XY Plane From SR, HIP, and Fully Heat-treated (SR+HIP+SOL+AGE) Sample (Machine Manufacturer – M 290).
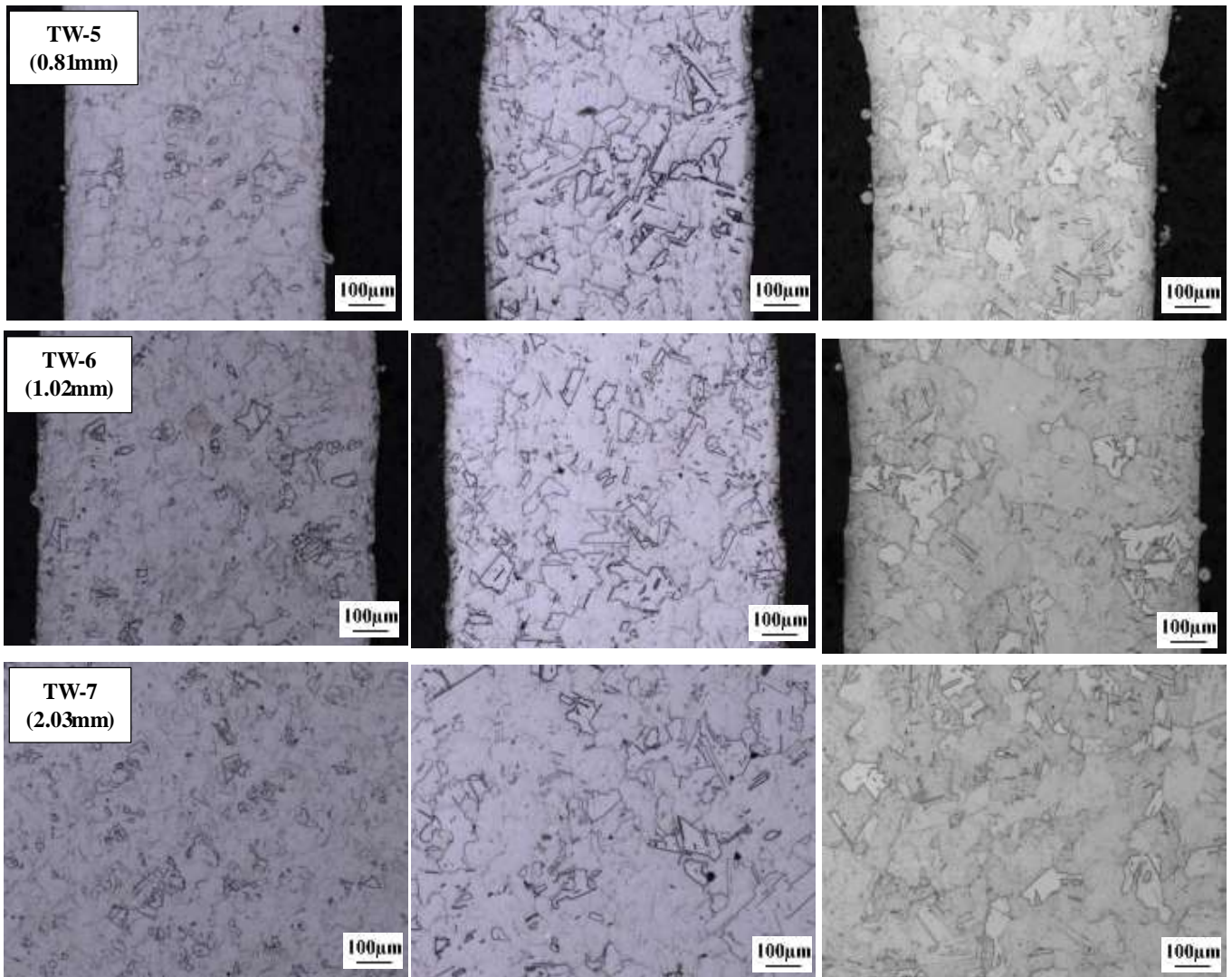
(Continued) Fig 3: Microstructural comparison of XY Plane From SR, HIP, and Fully Heat-treated (SR+HIP+SOL+AGE) Sample (Machine Manufacturer – M 290).

	SR Sample (1066°C for 1.5 h)	**HIP Sample** (SR+ 1163 °C for 3-4 h)	**Fully Heat-treated Sample** (SR+HIP+SOL+AGE)
TW-1 (0.10mm)			
TW-2 (0.20mm)			
TW-3 (0.41mm)			
TW-4 (0.61mm)			
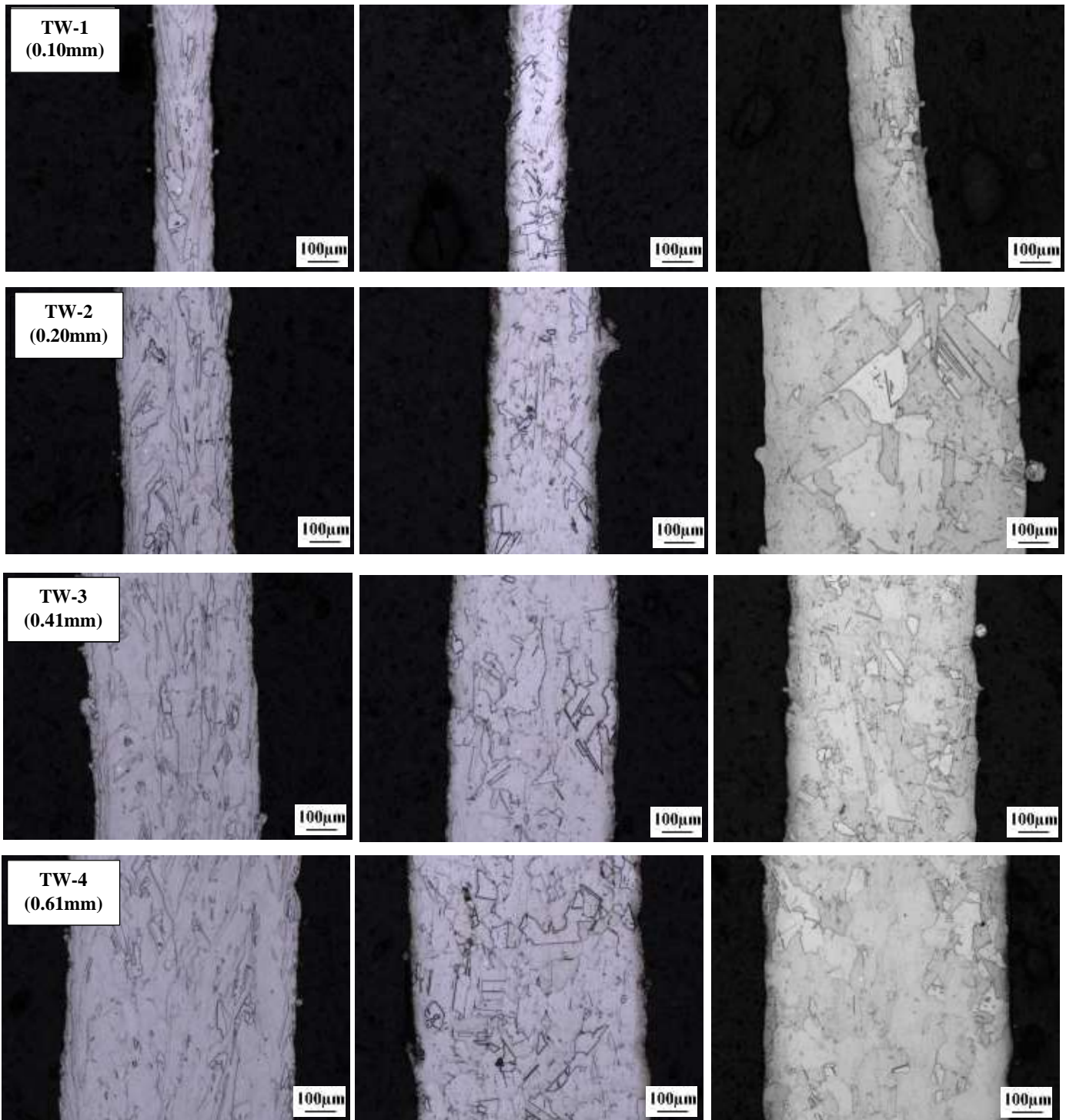
Fig 4: Microstructural comparison of YZ Plane From SR, HIP, and Fully Heat-treated (SR+HIP+SOL+AGE) Sample (Machine Manufacturer – M 290).

(Continued) Fig 4: Microstructural comparison of YZ Plane From SR, HIP, and Fully Heat-treated (SR+HIP+SOL+AGE) Sample (Machine Manufacturer – M 290).

Table 4: Grain size measurement in Microns of XY plane from different thin wall thicknesses for sixteen fully heat-treated (SR+HIP+SOL+AGE) build plates (NT- Nominal Thickness).

| Identifier	Machine Model Type	Wall No.1 (NT-0.10mm)	Wall No.2 (NT-0.20mm)	Wall No.3 (NT-0.41mm)	Wall No.4 (NT-0.61mm)	Wall No.5 (NT-0.81mm)	Wall No.6 (NT-1.02mm)	Wall No.7 (NT-2.03mm)
1	EOS M400		30	61	49	59	73	74
2	EOS M280			45	51	61	69	89
3	EOS M280			44	59	59	51	76
4	EOS M290			34	55	48	53	95
5	EOS M280		31	34	47	42	44	89
6	EOS M280			48	65	56	54	93
7	Concept M2	30	64	36	54	61	55	77
8	M280			34	43	46	63	77
9	EOS 290		25	45	44	43	49	76
10	SLM280	42	38	45	62	70	65	87
11	SLM280-Dual	25	27	41	35	52	50	88
12	VELO 3D	25	21	27	54	73	69	80
13	EOS 290		24	34	48	52	47	68
14	EOS 290		24	34	59	46	40	62
15	EOS M280			38	58	45	46	72
16	EOS M290	21	47	52	57	59	67	80
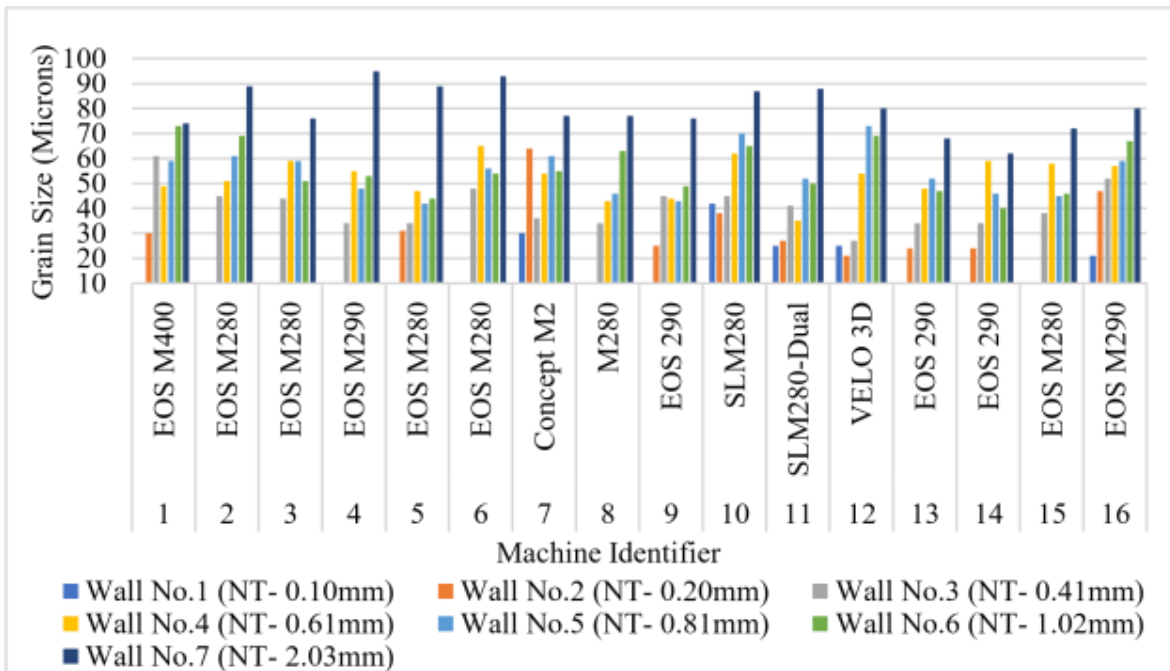
Fig 5: Average grain size comparison of XY plane for sixteen fully heat-treated (SR+HIP+SOL+AGE) thin wall samples.

Table 5: Grain size measurement in Microns of YZ plane from different thin wall thicknesses for sixteen fully heat-treated (SR+HIP+SOL+AGE) build plates (NT - Nominal Thickness).

Identifier	Machine Model Type	Wall No.1 NT-0.10m	Wall No.2 NT-0.20mm	Wall No.3 NT-0.41mm	Wall No.4 NT-0.61mm	Wall No.5 NT-0.81mm	Wall No.6 NT-1.02mm	Wall No.7 NT-2.03mm
1	EOS M400		56	65	80	67	61	62
2	EOS M280			50	57	36	80	85
3	EOS M280			43	61	53	47	80
4	EOS M290			51	40	59	56	77
5	EOS M280		33	33	44	41	46	81
6	EOS M280			37	62	58	58	78
7	Concept M2	44	58	43	46	60	74	60
8	M280			26	37	65	53	78
9	EOS 290		34	46	48	47	47	71
10	SLM280	46	57	52	60	73	71	76
11	SLM280-Dual	30	43	47	46	52	52	66
12	VELO 3D	25	30	28	45	72	62	75
13	EOS 290		35	31	58	54	48	84
14	EOS 290		33	43	51	56	41	89
15	EOS M280			48	47	56	40	71
16	EOS M280		45	46	67	90	59	87
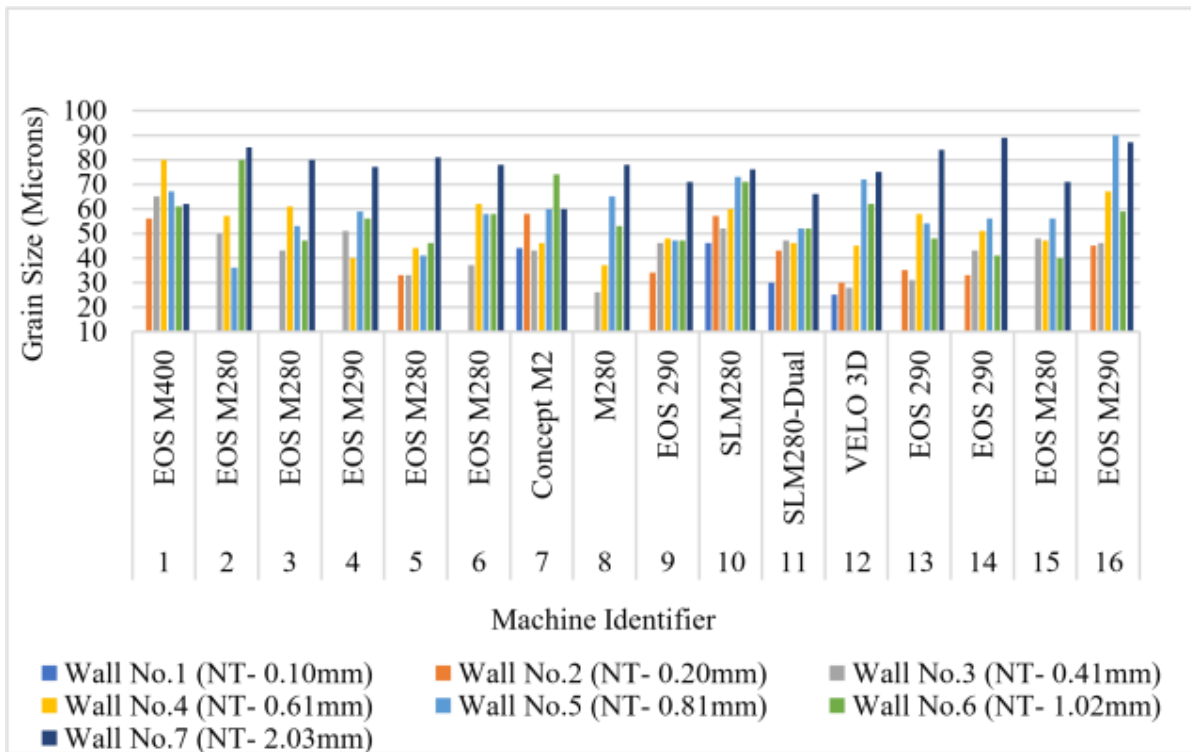
Fig 6: Average grain size comparison of YZ plane for sixteen fully heat-treated (SR+HIP+SOL+AGE) thin wall samples.

3.2 EBSD analysis of fully heat-treated (FHT) thin feature sections

Figures 7 to 14 illustrate EBSD inverse pole figure (IPF) grain orientation color maps [32] showing grain structure images for 4 different FHT, machine-built thin feature sections: Sample 7, CONCEPT M2; Sample 10, SLM 280; Sample 12, VELO 3D; and Sample 16, M290, as listed in Table 1; in both the XY and YZ plane build orientations. These comparative images are more clarified than the optical micrographs for the M290 machine build (Sample 16 in Table 1) and show the grain structure and grain size evolution, including annealing twin evolution with increasing feature section thickness. Figures 7 and 8, corresponding to CONCEPT M2 machine-built feature plate thin sections, show some remnants of columnar grain structures, especially fine grain sizes at the surface in TW-1 to TW-3 images observed in the XY plane (Fig. 7), and the corresponding columnar grains in TW-3 image observed in the YZ plane (in the build direction) (Fig. 8). Similar grain structure features are also evident in the Sample 10 SLM 280 machine (Table 1) builds in Figs. 9 and 10, especially for the thinner sections.

It can be especially noticed in Figs. 11 and 12, corresponding to feature build in the VELO 3D (or Sample 12, Velo Sapphire machine in Table 1), that significant columnar grain structures persist after FHT, especially for the feature thicknesses < 0.4 mm. This distinct microstructure observation is unique to this machine configuration which uses a contactless recoater. In addition, the process parameters for this machine are not given (Table 1), and it can only be assumed that the as-built microstructure consisted of very small columnar grain widths which do not readily recrystallize, even at the HIP temperature of 1163 ℃, although these columnar grain remnants are intermixed with recrystallized grains and annealing twins which evolve with increasing feature section thickness. This variance in grain size and structure is also reflected in comparing the grain size bar graphs in Figs. 5 and 6.

Figures 13 and 14 show the EBSD grain structure images corresponding to the optical microscope images in Figs. 3 and 4 for the FHT feature thickness sections produced in machine Sample 16 (M290) (Table 1). In contrast to the VELO 3D machine-related grain structures shown in Figs. 11 and 12, these thickness sections exhibit fully recrystallized and growing grains containing annealing twins. As shown previously in Tables 4 and 5 and in the accompanying grain size bar graphs in Figs. 5 and 6, respectively, for image views in the XY and YZ planes, the grain sizes are generally equiaxed and increase in size with increasing feature thickness. It is especially notable that the twin density decreases significantly from TW-4 to TW-7 [34].

In looking at Tables 4 and 5 in retrospect, it can be observed that between TW-3 and TW-6 (0.4 mm to 1.02 mm), the grain sizes for all L-PBF machine fabricated and FHT feature plate thin sections only increased by roughly 20 % overall, while between TW-6 and TW-7 (1.02 mm to 2.03 mm) the grain size nominally increased by more than 30 % for both the XY and YZ plane orientations. This occurs because of the grain growth associated with the higher heat-retaining volume which essentially characterizes the bulk feature plate sections.
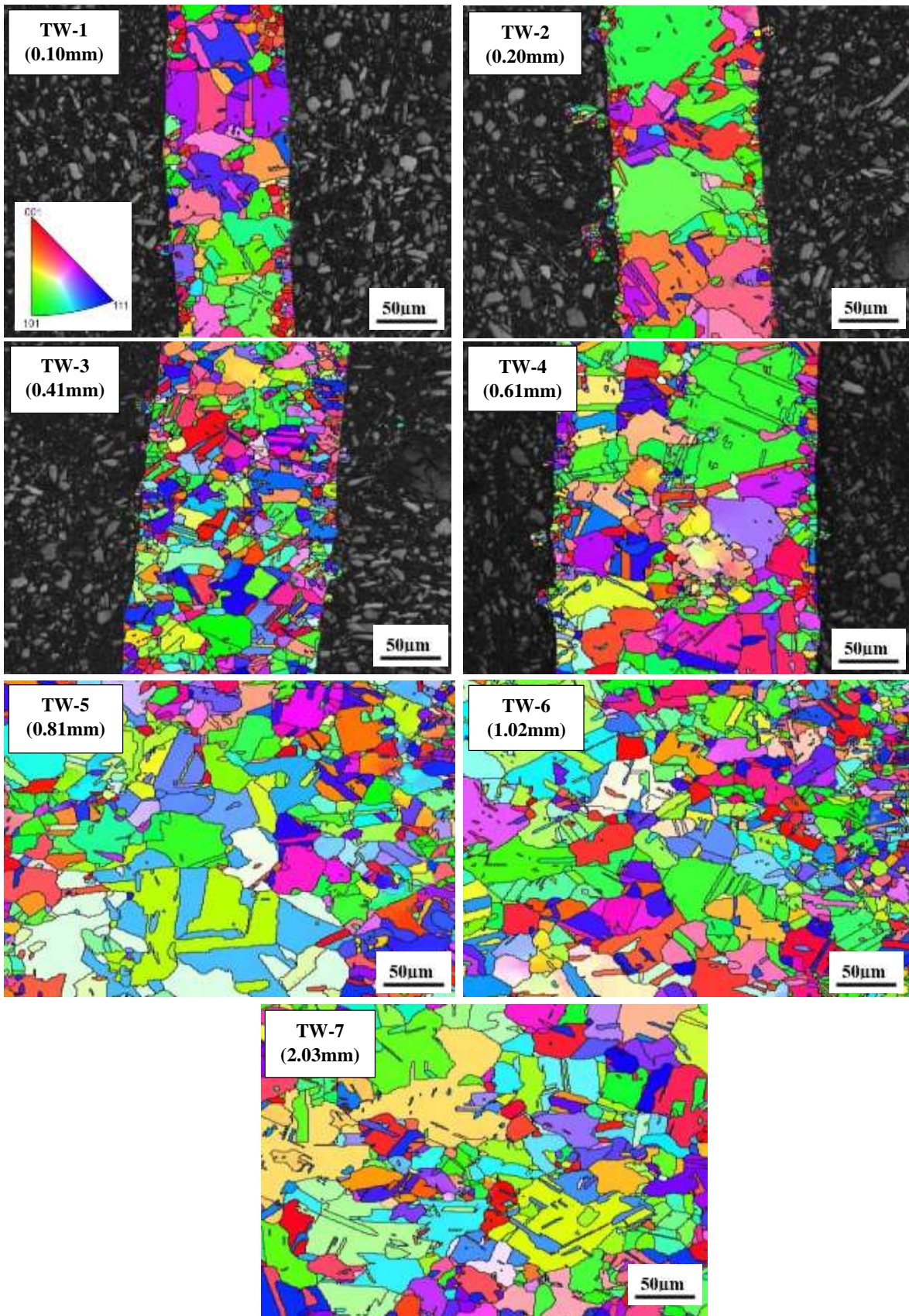
Fig 7: EBSD Analysis of XY plane of thin walls from fully heat-treated (SR+HIP+SOL+AGE) Sample 7 (Concept M2).
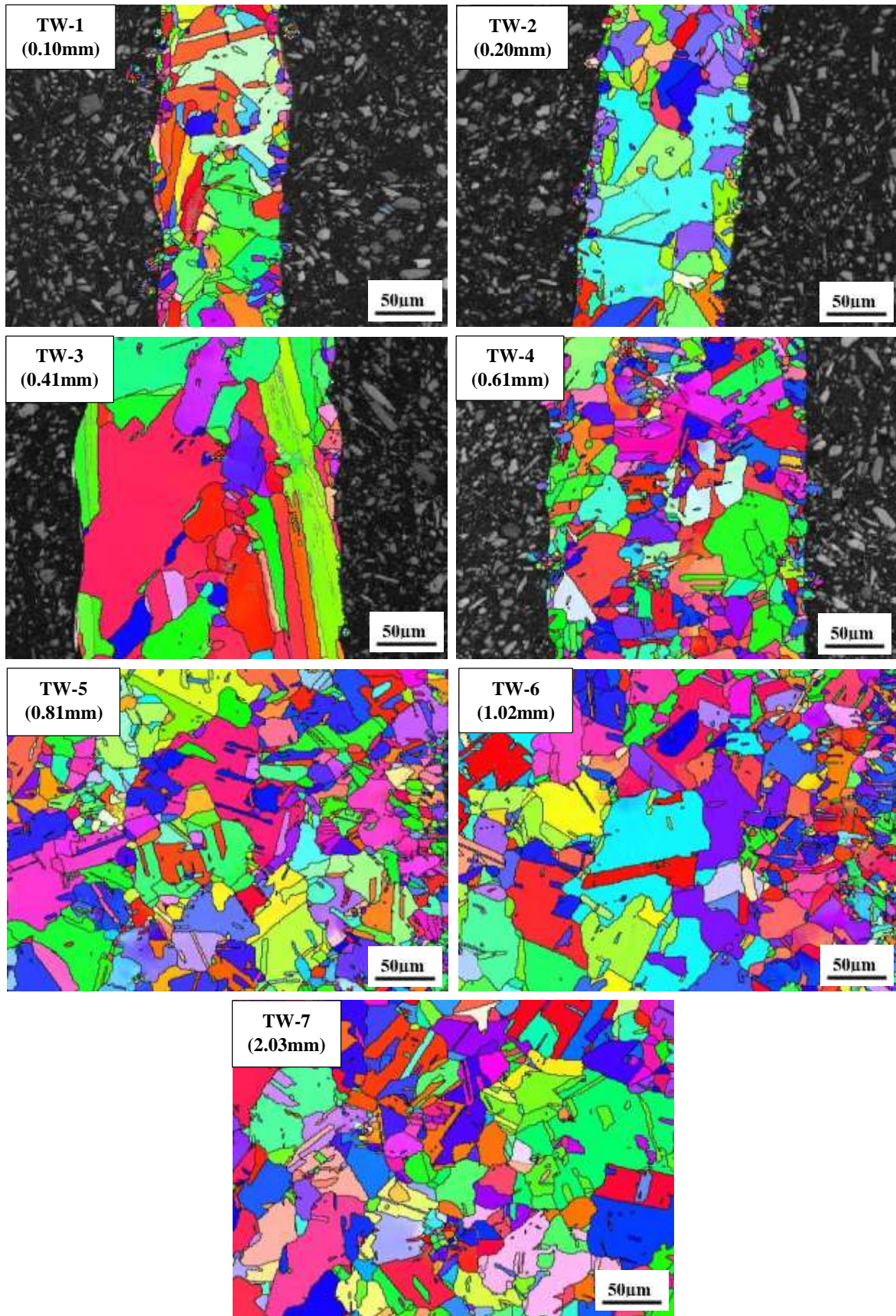
Fig 8: EBSD Analysis of YZ plane of thin walls from fully heat-treated (SR+HIP+SOL+AGE) Sample 7(Concept M2).
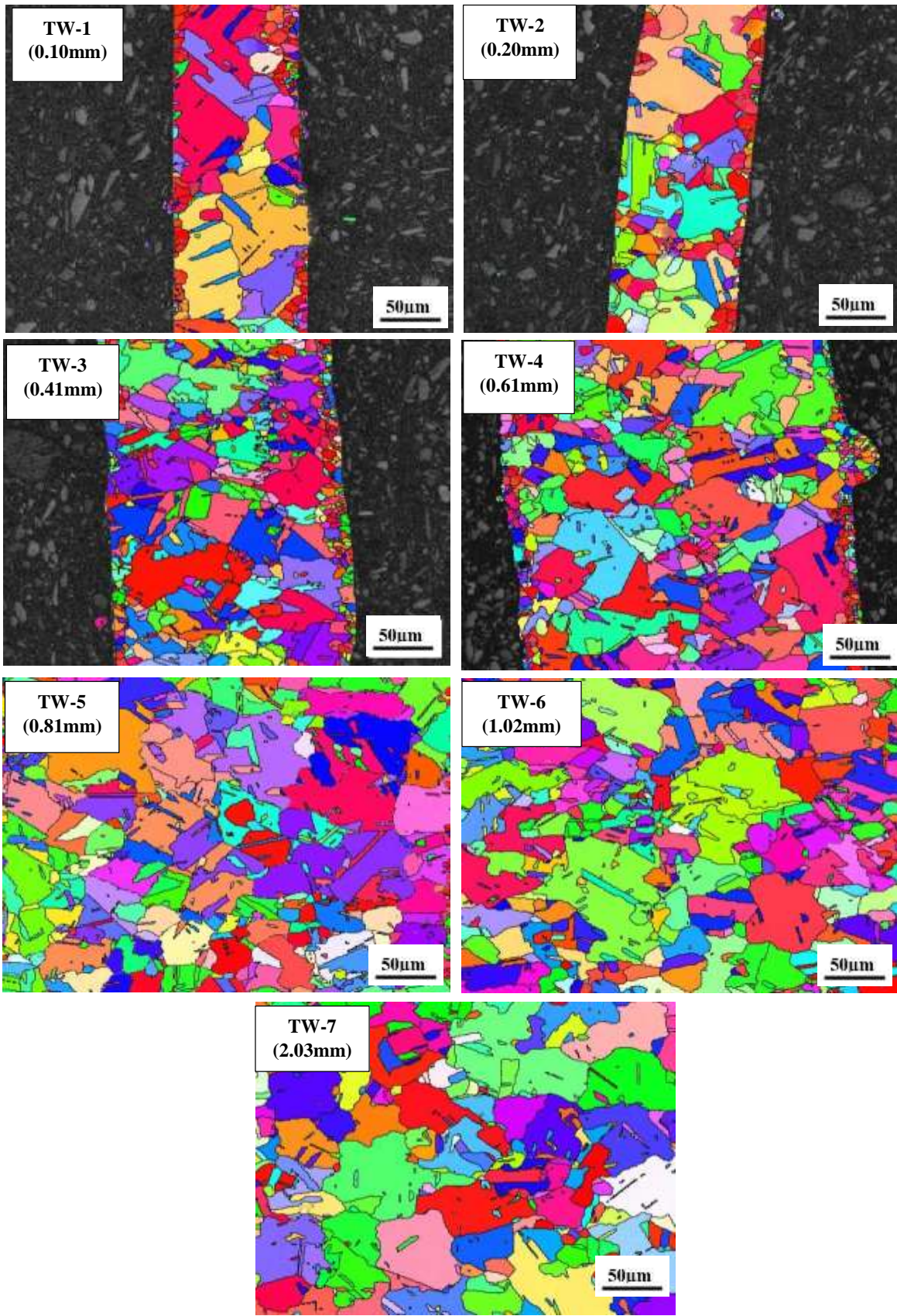
Fig 9: EBSD Analysis of XY plane of thin walls from fully heat-treated (SR+HIP+SOL+AGE) Sample 10 (SLM 280).
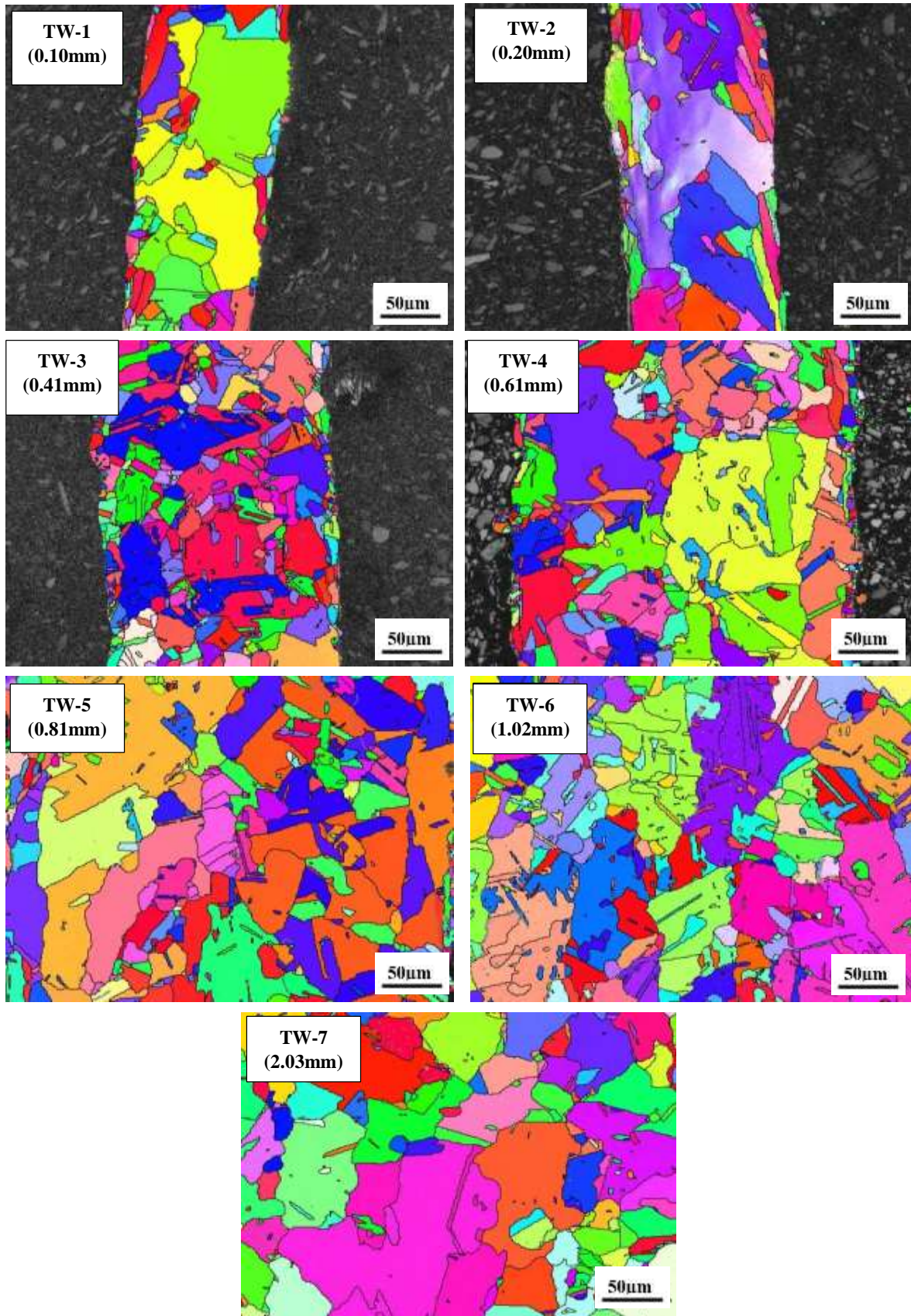
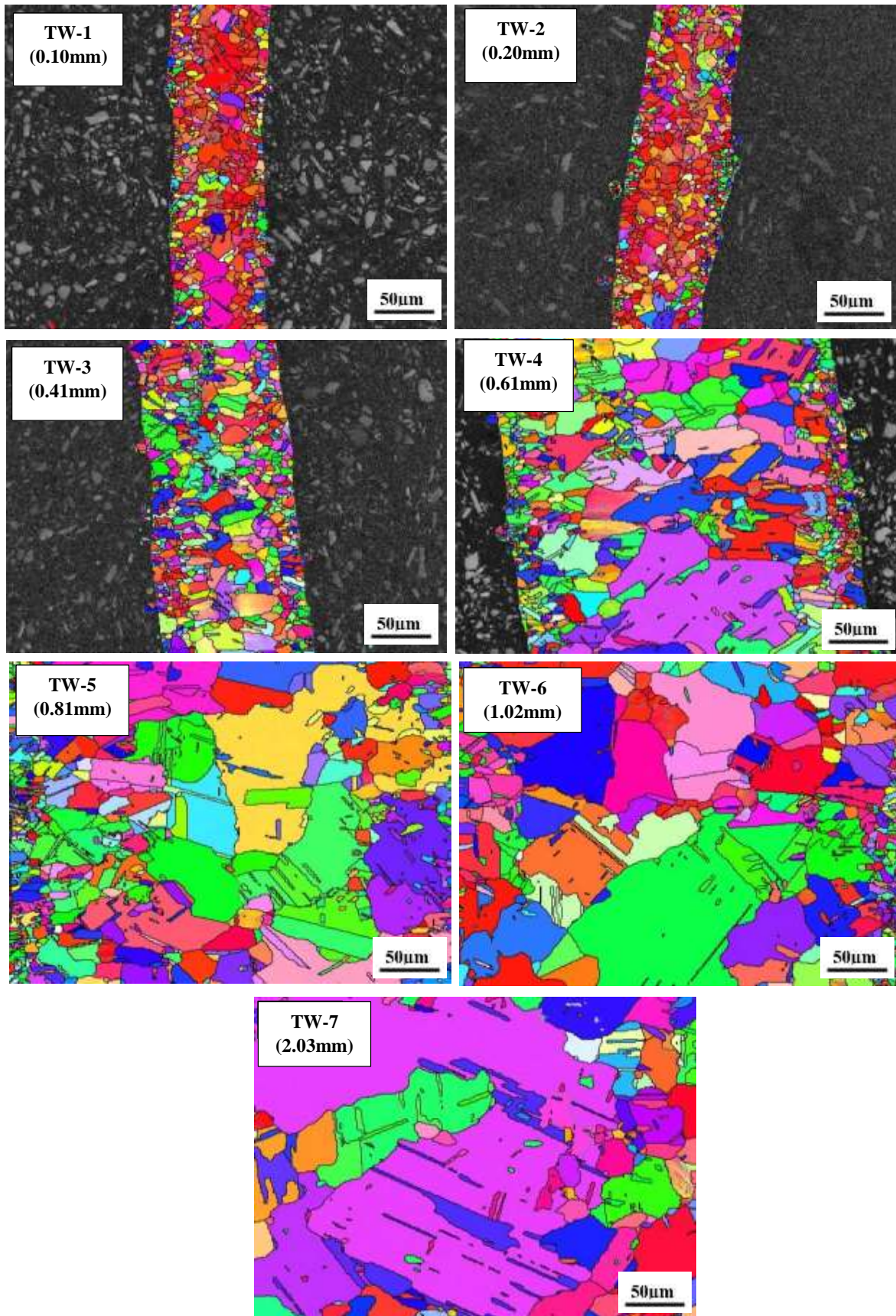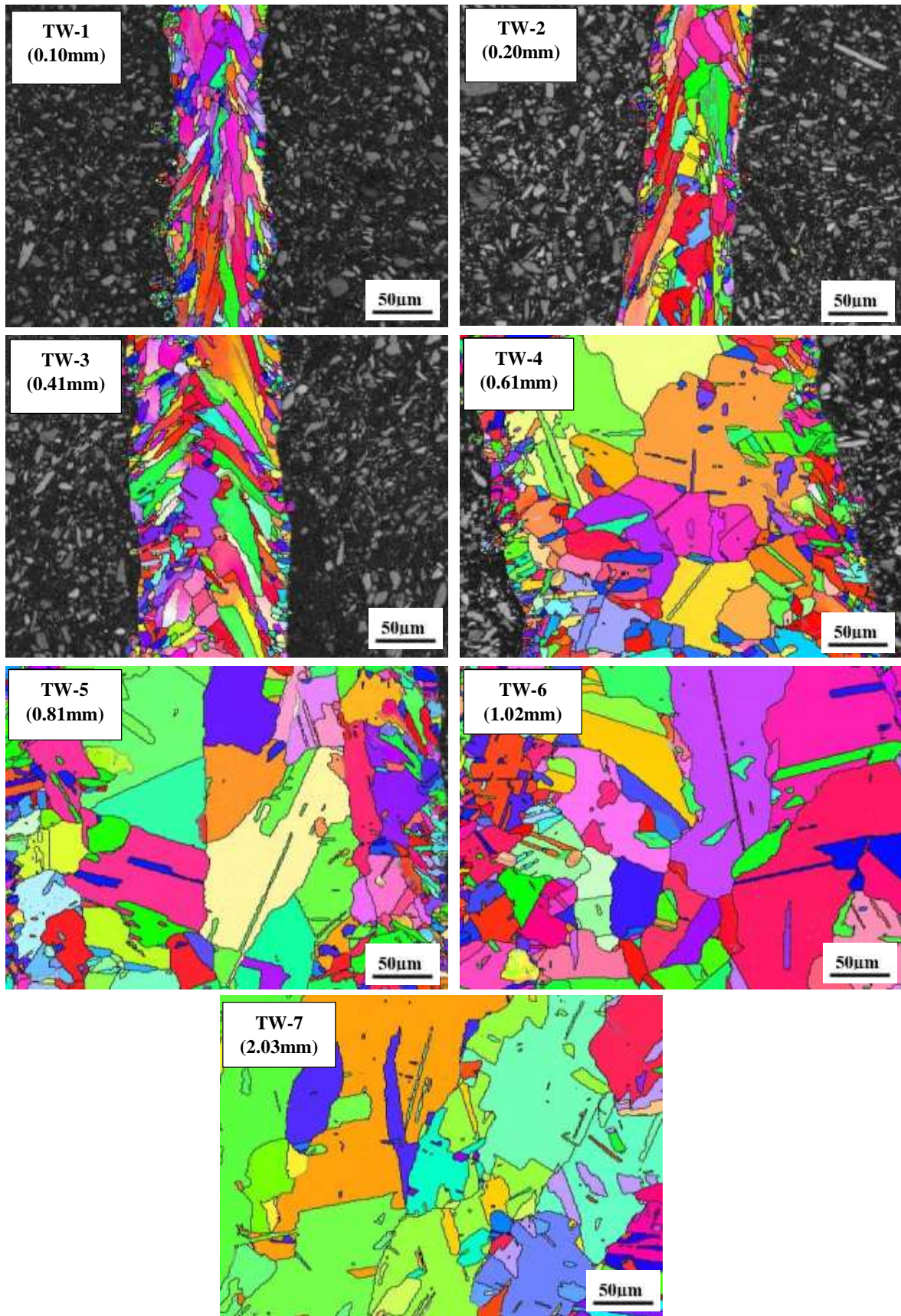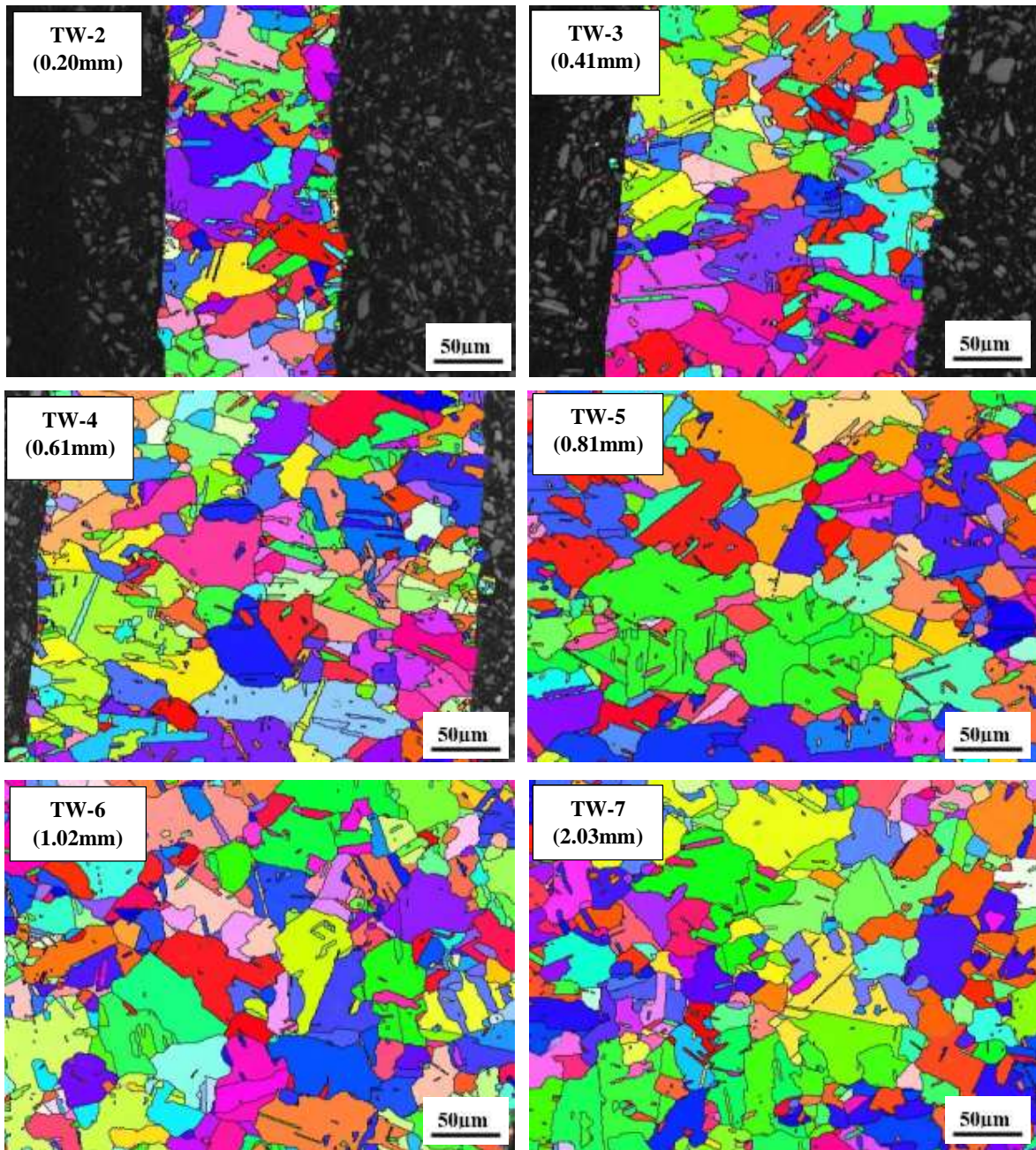**Fig 10:** EBSD Analysis of YZ plane of thin walls from fully heat-treated (SR+HIP+SOL+AGE) Sample 10 (SLM 280).

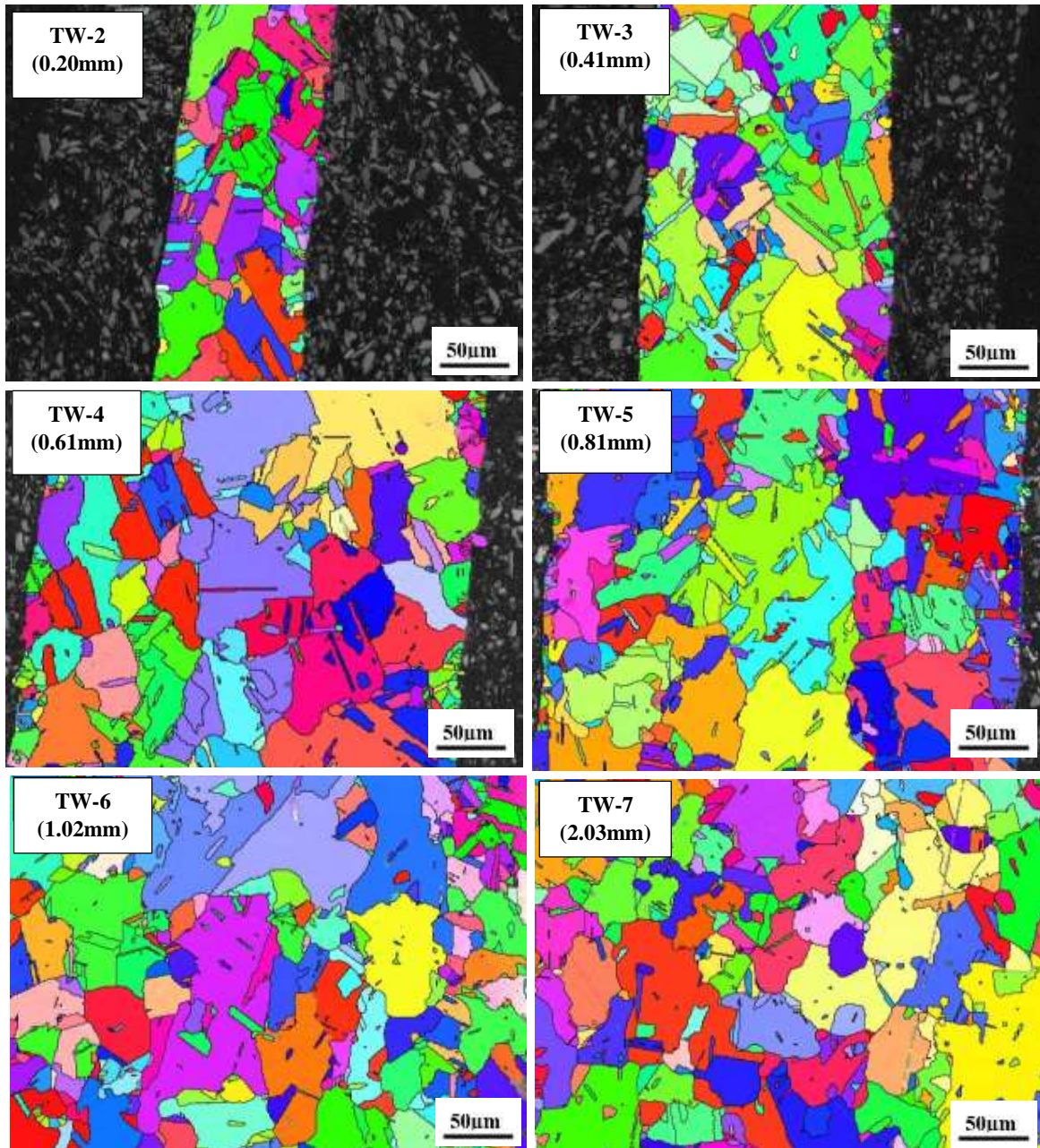**Fig 11:** EBSD Analysis of XY plane of thin walls from fully heat-treated (SR+HIP+SOL+AGE) Sample 12 (VELO 3D).

Fig 12: EBSD Analysis of YZ plane of thin walls from fully heat-treated (SR+HIP+SOL+AGE) Sample 12 (VELO 3D).

Fig 13: EBSD Analysis of XY plane of thin walls from fully heat-treated
(SR+HIP+SOL+AGE) Sample 16 (M290).

Fig 14: EBSD Analysis of YZ plane of thin walls from fully heat-treated (SR+HIP+SOL+AGE) Sample 16 (M290).

3.3 Vickers microindentation hardness measurements and analysis

The average Vickers microindentation hardness (HV) measured for each of the thin section features composing the L-PBF vender machine manufactured and fully heat-treated (FHT) geometric build plates (Figs. 1 and 2) is compared in the bar graphs in Figs. 15 and 16 corresponding to the XY and YZ plane orientations, respectively. Although there are some notable irregularities in the average hardness values for each thickness section, the hardness generally shows a trend of increasing with increasing section thickness. The hardness change from TW-2

(0.2 mm) to TW-3 (0.41 mm) averaged nominally 7% increase, while the increase from TW-6 (1.02 mm) to TW-7 (2.03 mm) averaged 2 %; and there was little change between TW-3 and TW-6 thicknesses.
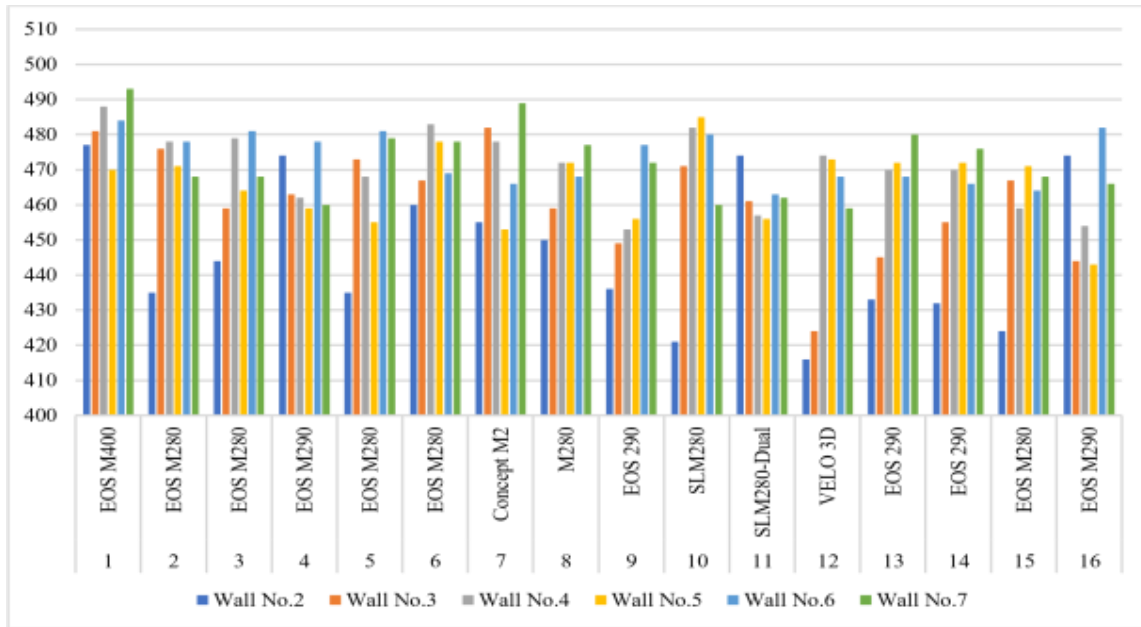

Fig 15: Microhardness comparison of XY plane for all sixteen fully heat-treated (SR+HIP+SOL+AGE) thin wall samples.
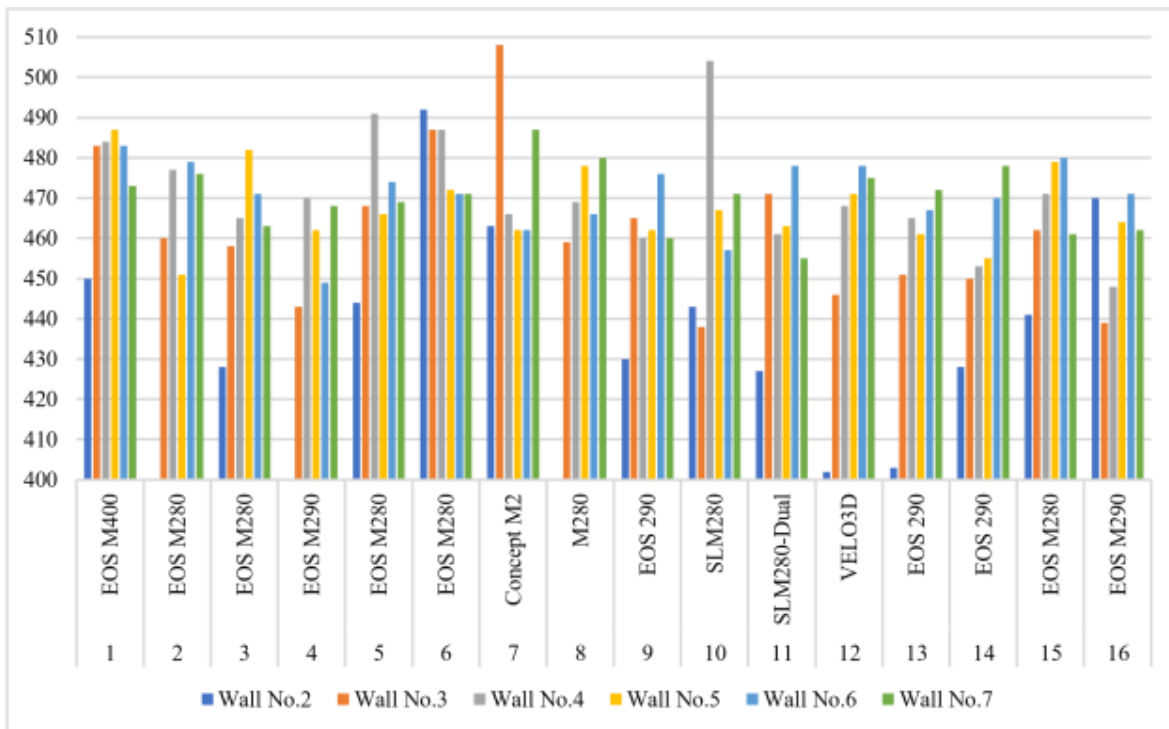

Fig 16: Microhardness comparison of YZ plane for all sixteen fully heat-treated (SR+HIP+SOL+AGE) thin wall samples.

While Figs. 15 and 16 show only the hardness (HV) averages for the FHT geometric build plates, Table 6 compares these hardness averages for the thickness sections (TW-2 to TW-7) variously heat treated: SR and SR + HIP; for machine Sample 16 (M290) (Table 1). This example corresponds to images in Figs. 3 and 4, and 13 and 14, for XY and YZ plane orientations, respectively. These averages increase by roughly 1 % from TW-3 to TW-7 for the SR and SR + HIP treatments in both the XY and YZ orientations, while the corresponding increase for the FHT samples is roughly 5 %. In this regard, it can be noticed in retrospectively examining the grain sizes for these various feature thicknesses in Tables 4 and 5 that there is generally an increase in the average grain size with increasing thickness; with the largest increase occurring for the thickest (2.03 mm) section. The average hardness for all FHT thin section measurements (Figs. 15 and 16) was ~HV 462 for thicknesses ranging from TW-3 to TW-7 (0.41 mm t0 2.03 mm), while for TW-2 thick sections (not included in Table 6) averaged ~ HV 445. It is also observed in Table 6 that the hardness average for all wall thicknesses in the XY plane increased by 21 % from the SR treatment to the HIP treatment and 13 % from the HIP treatment to the FHT treatment, corresponding to a hardness change of 34% from the SR treatment to the FHT treatment. Similar increases are observed for the heat treatments examined in the YZ orientation.

Table 6: Microhardness Comparison in Vickers Hardness (HV) among SR, HIP, & fully heat-treated thin wall samples from M290.

|	SR (1066°C for 1.5 h)		HIP (SR+ 1163 °C for 3-4 h)		Fully heat-treated (SR+HIP+SOL+AGE)	
Wall No.	**XY**	**YZ**	**XY**	**YZ**	**XY**	**YZ**
3 (0.41mm)	320	386	390	334	444	439
4 (0.61mm)	325	398	400	336	454	448
5 (0.81mm)	329	408	409	335	443	464
6 (1.02mm)	353	411	415	338	482	471
7 (2.03mm)	352	419	410	362	466	462

It is interesting to note that the increasing grain size with geometric feature plate section thickness (t) artifacts observed in this study (Tables 4 and 5) coincides with a generally increasing hardness for the FHT samples (Figs. 15 and 16), and this would seem to present a fundamental materials anomaly, since increasing grain size in bulk metals and alloys is characteristic of decreasing strength (yield stress (YS): where in the Hall-Petch relationship, YS ~ $d^{-0.5}$ [35], and UTS), and increasing ductility, or elongation. It is also important to recall that hardness, especially Vickers hardness (HV), is generally related to the yield stress (YS) through the relationship: YS ~ HV/3 [36,37]. There are two important reasons for this observation. First is the well-known exception for thin sections of metals and alloys, especially face-centered cubic metals and alloys. In this context, the thickness of sheet components along with the corresponding grain size has an effect on the mechanical properties, particularly tensile and creep-rupture behavior. For example, nominal bulk tensile behavior as a rule -of -thumb requires a thickness/grain size (t/d) ratio ranging from ~ 7 to 10 [18-20], while in the creep-rupture performance of Inconel 740H the critical value for t/d was

found to be 10 [38]. Yang and Lu [22] studied copper fabricated by electron beam melting (EBM) and found that while the yield stress was little affected by component thickness from 0.1 mm to 2 mm as in the present work, the UTS and elongation increased with thickness up to a critical value of t/d ~12. Koyama, et al. [19] showed that the yield strength decreased below a critical thickness for sheets of 316L stainless steel, and that the relation between the component thickness and the average grain size was a controlling factor. Raulea, et al. [21] found that for aluminum sheets, the critical thickness was above a t/d ratio of 20. Leicht, et al. [28] showed that L-PBF fabricated 316L stainless steel parts having a thickness of 1 mm exhibited a lower yield stress than 3mm thickness parts where the yield stress was similar to bulk dimensions. Farden, et al. [39] found that LPBF-fabricated Inconel 939 thin-walled structures exhibited an increase in the yield stress with increasing thickness for thicknesses of 0.5, 1, and 2mm: from 699 MPa to 987 MPa; with a corresponding increase in the elongation from 9 % to 14 %. Yang, et al. [22] concluded that on examining thin walled Cu components, thickness effects were governed by competition between dislocation activities in the interior grains and the surface grains up to some critical thickness where the bulk grain structure was controlling. This feature implies that dislocation emission from the specimen surface (solid-vapor interface) and interactions with the dislocation ledge emission at grain boundaries (solid-solid interface) is a critical factor in determining the mechanical properties, including hardness, of thin sections below some critical thickness [35,40,41].

   The second reason for the increasing hardness with increasing grain size and increasing section thickness shown on comparing Figs. 5 and 6 and 15 and 16 for the FHT Inconel 718 thickness artifacts L-PBF-manufactured by a range of commercial machines (Table 1) in this study is the creation of a uniform precipitation of nano-size gamma double-prime (Ni_3Nb) precipitates by the double aging process within the homogenized grain structure. Figure 17(a) shows a magnified view of the typical FHT grain structure exhibiting coarse precipitates and a uniform mottled grain distribution of the gamma double-prime nanoprecipitates which are confirmed to have a volume fraction of 3-4 percent as shown in the XRD spectra in Fig. 17(b); corresponding to similar studies of double-aged Inconel 718 [42,43]. The precipitation hardening tends to dominate the larger grain structures for thicker sections and the bulk volume, since the hardness values become fairly consistent for the thickness artifacts greater than 0.4 mm as shown in Figs. 15 and 16, and Table 6 for the FHT samples; although variations in hardness range from ~ HV 450 to HV 505 in both the XY and YZ plane orientations, consistent with the measured bulk hardness values which ranged from ~ HV 480 to HV 502. These hardness range are consistent with average values of HV 450 in the L-PBF and heat -treated Inconel 718 study by Tucho, et al. [13], HV 467 after double aging in the L-PBF fabrication of Inconel 718 in the study by Zhou, et al. [44], and HV 470 in the LPBF-fabrication and heat treatment of Inconel 718 in the study by Jiang, et al. [45].
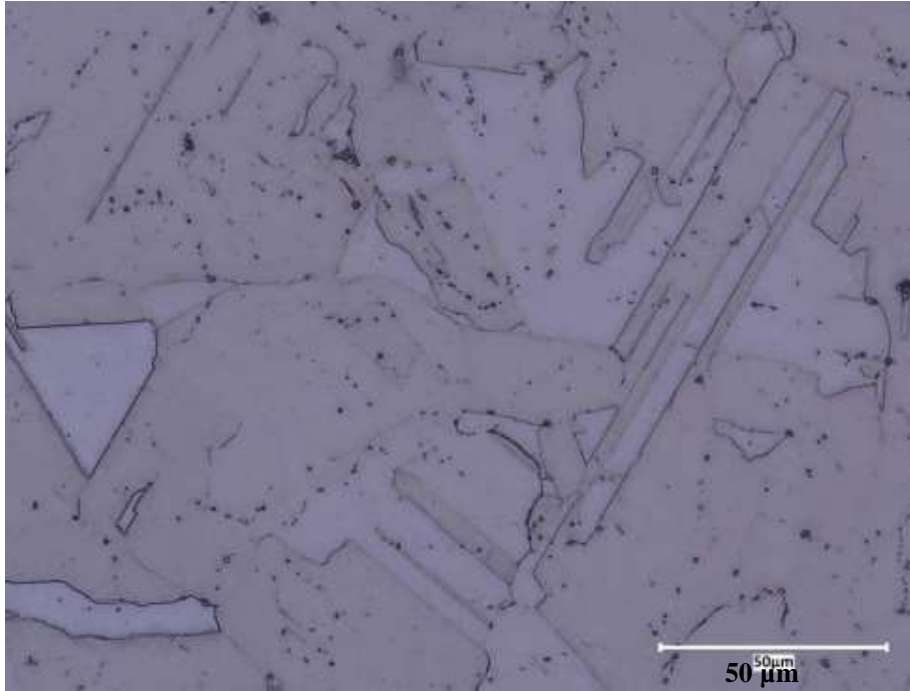
(a)
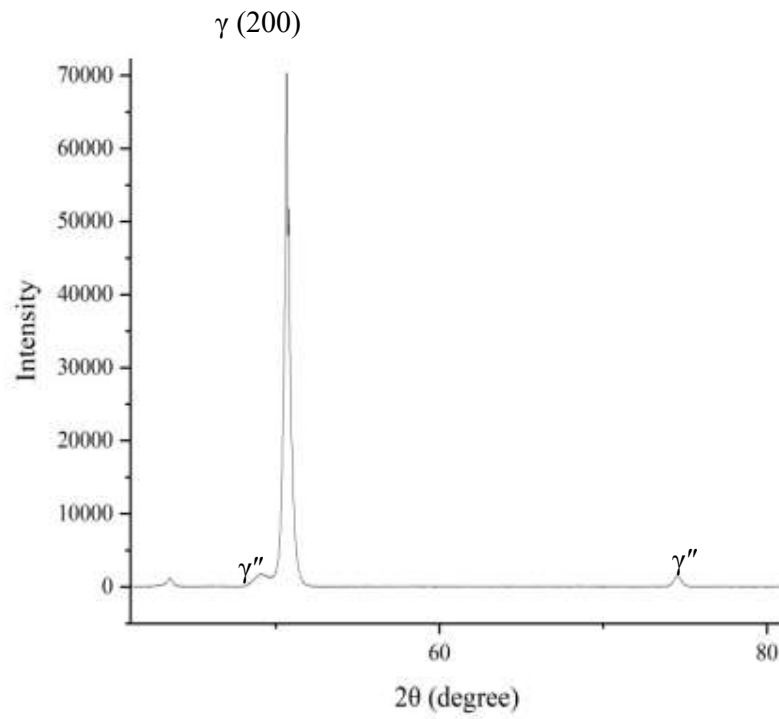
(b)

Fig 17: (a) Higher magnification optical microscopic image and (b) XRD spectrum in YZ plane for EOS M290, showing gamma double -prime precipitation.

The bar graph comparisons in Figs. 15 and 16 provide an overview of microindentation hardness (HV) trending for the experimental thickness sections for fully heat treated (FHT) geometric build plate artifacts fabricated in a wide range of LPBF machine configurations as noted (see also Table 1). Figure 18 illustrates for comparison whisker box plots (also referred to as box plots or box-whisker plots) [46,47] summarizing all of the microindentation hardness data shown in the bar graphs of Figs. 15 and 16 for section thicknesses both in the XY and YZ plane orientations, respectively. These plots (Fig. 18 (a) and (b)) graphically depict the median, upper and lower quartiles, and upper and lower extremes of the corresponding hardness data sets in Figs. 15 and 16. It can also be noted in these summary plots (Fig. 18) that there is little hardness variation (HV) for thicknesses TW-4 to TW-7 (or nominal thicknesses of 0.6 to 2.0 mm) where the mean hardness can be observed to be HV 472 in both the XY and YZ plane orientations; with a variance of HV 5. Notice that t/b ~ 10 for thicknesses of 0.6 mm and greater. The Vickers microindentation hardness for wall 3, TW-3 (0.4 mm nominal thickness) drops to ~ HV 460 in Fig. 18 (a) and (b), and even lower for TW-2 (0.2 mm nominal thickness); indicating that the microstructure and corresponding hardness for part thicknesses below ~ 0.6 mm exhibit a lower confidence in LPBF machine reproducibility for complex Inconel 718 alloy manufactured parts; consistent with the conclusions of Gradl, et al [29] who concluded that relative error for the range of L-PBF machines used in this study (Table 1) increases with decreasing feature size, particularly part thickness.
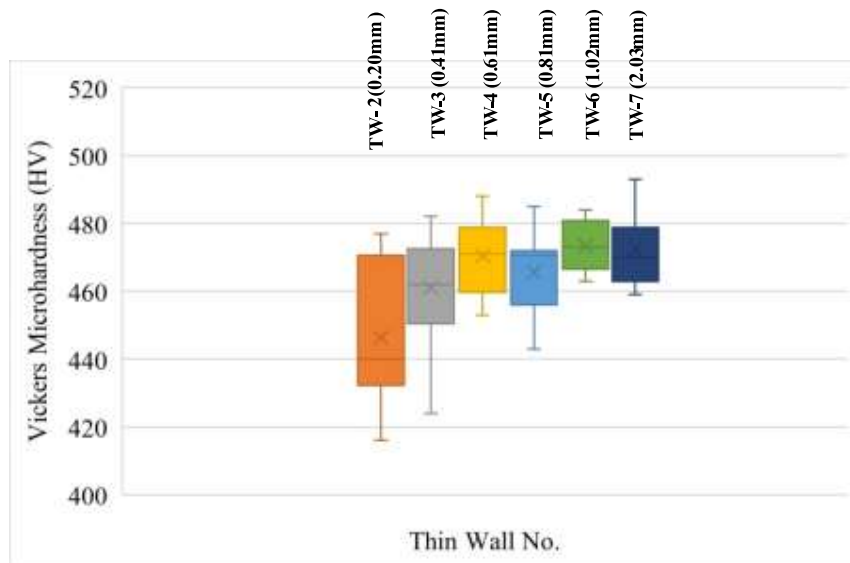
(a)
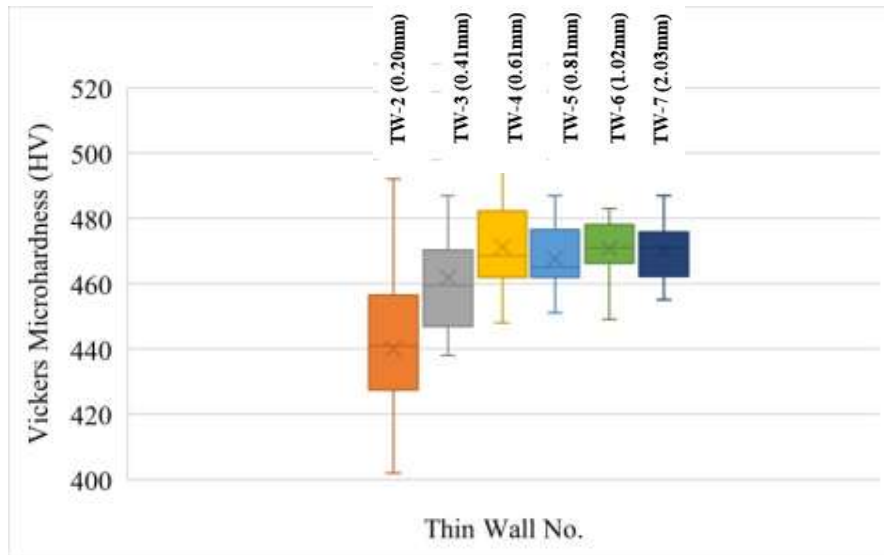
(b)

Figure 18: Whisker plot for microhardness comparison in (a) XY plane and (b) YZ
plane for sixteen fully heat-treated (SR+HIP+SOL+AGE) samples.

4. Summary and conclusions

   The ability to qualify the building of various thin section thicknesses is particularly important in
the fabrication of complex parts by L-PBF additive manufacturing of high-temperature and high-
performance superalloys such as Inconel 718 used in aerospace and gas turbine industries. Products
and components having complex geometries with thin walls such as cooling channels and related
heat transfer features with dimensions below about 0.4 mm are especially vulnerable to build errors
in commercial L-PBF machines. Control of geometry and its related microstructure and mechanical
properties is necessary for assuring a requisite design strategy and end-use performance; and the
practical limitations of the various L-PBF machine configurations. While the previous, companion
studies by Gradl, et al [29] compared the dimensional accuracy and consistency across a variety of
LPBF machine configurations, including various thin wall thickness, the present work examined
these thin walled thickness features by observing the associated microstructures (by optical
microscopy and EBSD mapping) as well as the corresponding Vickers microindentation hardness
(HV).

   This study utilized a series of 16 geometric build plates manufactured in the original work by
Gradl, et al. [29] (Fig. 1) using an identical CAD file across 15 different L-PBF additive
manufacturing machines installed at 12 different vender locations. In the present work, these build
plates were variously heat treated by stress relief (SR) anneal at 1066 $^{\circ}$C , SR + HIP at 1163 $^{\circ}$C,
and a fully heat treated (FHT) regimen consisting of SR + HIP + solution (SOL) treatment at 1066
$^{\circ}$C followed by double aging at 760 $^{\circ}$C and 649 $^{\circ}$C. The FHT regimen produced a homogeneous,
generally equiaxed grain structure precipitation hardened by gamma double-prime (Ni$_3$Nb)
nanoprecipitates. Seven different wall thickness features ranging from nominally 0.1 mm to 0.2
mm were specifically studied in this work. Component thicknesses below ~ 0.2 mm were not
consistently reproduced, while the grain size and microindentation hardness were observed to
increase with increasing thickness up to ~ 0.6 mm, where the hardness tended to stabilize at ~ HV

472; consistent with the hardness for commercially produced and heat treated (including double aging) Inconel 718 products.

The major conclusions in this study included the following:

- Feature thickness below ~ 0.4 mm did not print reproducibly across all LPBF machine configurations in fabricating geometric build plates of Inconel 718 alloy.

- Fully heat-treated (FHT) thickness feature components of LPBF manufactured Inconel 718 ranging from nominal 0.1 mm to 2.0 mm exhibited generally increasing, equiaxed grain structures containing annealing twins, which ranged in size from ~ 21 microns to ~ 93 microns. Surface effect competition with internal grain structure resulted in increasing Vickers micro indentation hardness in the thickness range of ~ 0.1 mm to ~ 6 mm; where the hardness stabilized at ~ HV 472 as a result of gamma double-prime nanoprecipitation hardening, a hardness consistent with commercially heat- treated Inconel 718 products.

- The grain structure(size) and corresponding Vickers hardness exhibited some anisotropy when measured in the XY plane perpendicular to the build direction in contrast to the YZ plane parallel to the build direction; typical for LPBF-manufactured components.

Conflicts of Interest: The authors declare no conflicts of interest.

References

[1]   T. Perela, J. V. Kennedy, J. Potgleter, A comparison of traditional manufacturing vs additive manufacturing: the best method for the job: Peocedia Manuf. 30 (2019) 11-18.
[2]   S. A. M. Tofail, E. P. Koumoulos, A. Bandyopadhyay, S. Bose, L. O. Donoghue, C. Charitidis, Additive manufacturing: scientific and technological challenges, market uptake and opportunities, Mater. Today 21 (2018) 22-37.
[3]   B. S. Rupal, N. Anwer, M. Secanell, A. J. Qurzshi, Geometric tolerance and manufacturing assemblability estimation of metal additive manufacturing (AM) processes, Mater. Design 194 (2020) 108842.
[4]   S. I. Sing, W. Y. Yeong, Laser powder bed fusion for metal additive manufacturing: perspectives on recent developments, Virtual Phys. Prototyp. 15 (2020) 359-370.
[5]   G. Ameta, R. Lipman, S. Moylan, P. Witherell, Investigating the role of geometric dimensioning and tolerancing in additive manufacturing, Int. J. Mech. Design Trans., 137, ASME, 2015.
[6]   M. Yakout, M. Elbestawi, S. C. Veldhuts, A review of additive manufacturing technologies, Solid State Phenom. 278 (2018) 1-14.

[7]   M. Baumers, P. Dickens, C. Tuck, R. Hague, Technological forecasting & social change. The cost of additive manufacturing: machine productivity, economies of scale, and technology push, Technol. Forecast . Soc. Change, 104 (2016) 193-201.

[8]   T. Debroy, H. I. Wei, J. S. Zuback, T. Mukherjee, J. W. Elmer, J. O. Milewski, Additive manufacturing of metallic components: process, structure, and properties, Prog. Mater. Sci. 92 (2018) 112-224.

[9]   J. P. Oliveira, A. D. Lalonde, J. Ma, Processing parameters in laser powder bed fusion metal additive manufacturing, Add. Manuf. 193 (2020) 1-12.

[10]   W. J. Sames, F. A. List, S. Pannala, R. R. Dehoff, S. S. Babu, The metallurgy and processing science of metal additive manufacturing, Int. Mater. Rev. 6608 (2016) 1-46.

[11]   L. E. Murr, A metallographic review of 3D printing/additive manufacturing of metal and alloy products and components, Metall. Microstruct. Anal. 7(2) (2018) 103-132.

[12]   D. Y. Zhang, W. Niu, X. Y. Cao, Z. Liu, Effect of standard heat treat on the microstructure and mechanical properties of selective laser melting manufactured Inconel 718 superalloy, Mater. Sci. Engr. A644 (2015) 32-46.

[13]   W. M. Tucho, P. Cuvillier, A. Sjolyst-Kverneland, V. Hansen, Microstructure and hardness studies of Inconel 718 manufactured by selective laser melting before and after solution heat treatment, Mater. Sci. Engr. A689 (2017) 220-232.

[14]   E. Chlebus, K. Griber, B. Kuznicka, T. Kurzynowski, Effect of heat treatment on the microstructure and mechanical properties of Inconel 718 processed by selective laser melting, Mater. Sci. Engr. A639 (2015) 647-655.

[15]   J. Schneider, B. Lund, M. Fullen, Effect of heat treatment variations on the mechanical properties of Inconel 718 selective laser melted specimens, Add. Manuf. 21 (2018) 248-254. [16] S. Raghaven, B. C. Zhang, P. Wang, C. N. Sun, M. L. S. Nai, T. Li, J. Wei, Effect of different heat treatments on the microstructure and mechanical properties in selective laser melted Inconel 718 alloy, Mater. Manuf. Processes 32 (2017) 1588.

[17] V. Luna. L. Trujillo, A. Gamon, E. Arrieta, L. E. Murr, R. B. Wicker, C. Katsarelis, P. R. Gradl, F. Medina, Comprehensive and comparative heat treatment of additively manufactured Inconel 625 alloy and corresponding microstructures and mechanical properties, J. Manuf. Mater. Process. 6 (2022) 107-125.

[18] E. Hug, C. Keller, Intrinsic effects due to the reduction of thickness on the mechanical behavior of nickel polycrystals, Metall. Mater. Trans. A41 (2014) 2498-2506.

[19] A. Kohyama, K. Hamada, H. Matsui, Specimen size effects on tensile properties of neutron irradiated steels, J. Nucl. Mater. 179-181 (1991) 417-420.

[20] S. Miyazaki, K. Shibata, H. Fujita, Effect of specimen thickness on mechanical properties of polycrystalline aggregates with various grain sizes. Acta Metall. 27 (1979) 855-862.

[21] L. V. Raulea, A. M. Goijaerts, L. E. Govaert, F. P. T. Baaijens, Size effects in the processing of thin metal sheets, J. Mater. Process. Technol. 115 (2001) 44-48.

[22] L. Yang, L. Lu, The influence of sample thickness on the tensile properties of pure Cu with different grain sizes, Scripta Mater. 69 (2013) 242-245.

[23] A. Leicht, U. Klemeni, E. Hryha, Effect of build geometry on the microstructural development of 316L parts produced by additive manufacturing, Mater. Charact. 143 (2018) 137143.

[24] T. Niendorf, F. Brenne, M. Schaper, Lattice structures manufactured by SLM: on the effect of geometrical dimensions on microstructure evolution during processing, Metall. Mater. Trans. B45 (2014) 1181-1185.

[25] O. Scott-Emuakpor, T. George, E. Henry, C. Holycross, J. Brown, As-built geometry and surface finish effects on fatigue and tensile properties of laser fused Ti-6Al-4V, Proc. ASME Turbo Expo 6 (2017) 1-11.

[26] K. Senithilkumaran, P. M. Pandey, P. V. M. Rao, Influence of building strategies on the accuracy of parts in selective laser sintering, Mater. Design 30 (2009) 2946-2954.

[27] E. S. Kim, C. M. Karthik, K. R. Ramkumar, S. G. Jeong, R. E. Kim, G. H. Gu, H. S. Kim, Thickness effect on the microstructure, mechanical properties, and anisotropy of laser-powder bed fusion processed 316L stainless steel, J. Mater.Sci. 57 (2022) 18101-18117.

[28] A. Leicht, C. Pauzon, M. Rashidi, U. Klement, L. Nyborg, E. Hryha, Effect of part thickness on the microstructure and tensile properties of 316L parts produced by laser powder bed fusion, Adv. Indust. Manuf. Engr. 2 (2021) 100037.

[29] P. R. Gradl, D. C. Tinker, J. Ivester, S. W. Skinner, T. Teasley, J L. Bili, Geometric feature reproducibility for laser powder bed fusion (L-PBF) additive manufacturing with Inconel 718, Add. Manuf. 47 (2021) 102305.

[30] M. J. Donachie, S. J. Donachie, Superalloys: A Technical Guide, 2nd Edition, 2002, ASM International, Materials Park, OH

[31] C. A. Schneider, W. S. Rasband, K. W. Eliceiri, NIH Image to Image J: 25 years of image analysis, Nat. Methods, 9(7) (2012) 671-675.

[32] F. J. Humphreys, Review grain and subgrain characterization by electron backscatter diffraction, J. Mater. Sci 36 (2001) 3833-3854.

[33] A. J. Schwartz, M. Kumar, B. L. Adams, D. P. Field (eds.), Electron Backscatter Diffraction in Materials Science, 2nd Edition, 2009, Springer, NY.

[34] Y. Jin, M. Bernacki, A. Agnoli, B. Lin, G. S. Rohrer, A. D. Rollett, N. Bozzolo, Evolution of the annealing twin density during delta-supersolvus grain growth in the nickel-base superalloy Inconel 718, Metals 6 (2016) 5-14.

[35] L. E. Murr, Handbook of Materials Structures, Properties, Processing and Performance, Vol. 1, Springer, NY, 2015.

[36] D. Tabor, The Hardness of Metals, Clatenden Press, Oxford, UK, 1951.

[37] J. B. Cahoon, W. H. Broughton, A. K. Kutzak, The determination of yield strength from hardness measurements, Metall. Trans. 2 (1971) 1975-1983.

[38] J. Shingledecker, E. Griscom, A. Bridges, Relationship between grain size and sample thickness on creep-rupture performance of thin metallic sheets of Inconel alloy 740H, J. Mater. Engr. Perform. Published online: 12 January (2023).

[39] A. Fardan, U. Klement, H. Brodin, E. Hryha, Effect of part thickness and build angle on the microstructure, surface roughness, and mechanical properties of additively manufactured IN-939, Metall Mater. Trans. A54 (2023) 1803-1814.

[40] L. E. Murr, Interfacial Phenomena in Metals and Alloys, Addison-Wesley Publishing Co, Reading, MA, 1975.

[41] L. E. Murr, S-H. Wang, Comparison of microstructural evolution associated with the stressstrain diagram for nickel and 304 stainless steel: an electron microscope study of microyielding and plastic flow, Res Mechanica 4 (1982) 237-274.

[42] L-S-B. Ling, Z. Yin, Z. Hu, J-H. Liang, Z-Y. Wang, J. Wang, B-D. Sin, Effects of gamma double-prime Ni_3Nb phase on mechanical properties of Inconel 718 superalloys with difrerent heat treatments, Materials 13 (2020) 151-165.

[43] X. Tao, J. Kavanagh, X. Li, H. Dong, A. Matthews, An investigation of precipitation strengthened Inconel 718 superalloy after triode plasma nitriding, Surf. Coatings Technol. 442 (2022) 128401.

[44] Le Zhou, A. Mehta, B. McWilliams, K. Cho, Y. Sohn, Microstructure, precipitates and mechanical properties of powder bed fused Inconel 718 before and after heat treatment, J. Mater. Sci. Technol. 35 (2019) 1153-1164.

[45] R. Jiang, A. Mostafaei, Z. Wu, A. Choi, P-W. Guan, M. Chmielus, A. D. Rollett, Effect of heat treatment on microstructural evolution and hardness homogeniaty in laser powder bed fusion of Inconel 718, 35 (2020) 101202.

[46] E. R. Tufte, The Visual Display of Quantitative Information, Graphics Press, Cheshire, CT, 2001.

[47] Y. Sun, M. C. Genton, Functional boxplots, J. Comp. Graphical Stat. 2011 (2012) 316-337.